

Friedrich Schiller Universität Jena  
PAF

Dissertation

**High-Fluence Ion Beam  
Irradiation of Semiconductor  
Nanowires**

Andreas Johannes

März 2015

# **Abstract**

Hier alles Bla

# Contents

<b>1</b>	<b>Introduction</b>	<b>1</b>
<b>2</b>	<b>Background</b>	<b>7</b>
2.1	Ion-solid interaction . . . . .	7
2.2	Simulation of ion-solid interaction . . . . .	16
<b>3</b>	<b>Experimental Methods</b>	<b>23</b>
3.1	Nanowire synthesis . . . . .	23
3.2	Modification . . . . .	25
3.3	Characterization . . . . .	26
<b>4</b>	<b>Sputtering of Nanowires</b>	<b>31</b>
4.1	First results in <i>Mn</i> irradiated <i>GaAs</i> . . . . .	31
4.2	Simulation results . . . . .	31
4.3	Redeposition . . . . .	33
4.4	<i>Si</i> nanowire sputtering by $Ar^+$ irradiation . . . . .	37
4.5	Discussion . . . . .	39
<b>5</b>	<b>High Doping Concentrations in Nanowires</b>	<b>40</b>
5.1	Doping and Sputtering . . . . .	40
5.2	Pseudo-dynamic simulation . . . . .	40
5.3	Results from optimal irradiation conditions . . . . .	40
5.4	Discussion of relevant effects . . . . .	40

*Contents*

<b>6 Plastic Flow in Silicon Nanowires</b>	<b>41</b>
6.1 Discovery . . . . .	41
6.2 Quantification of the Deformation . . . . .	42
6.3 Knock-on transport of mass . . . . .	44
6.4 Irradiation at large angles of incidence . . . . .	47
6.5 The deformation mechanism . . . . .	55
<b>7 Summary and Outlook</b>	<b>58</b>

# 1 Introduction

We are living in an era dominated by the information technology (IT). There is virtually no part of life not influenced by the continuing advances in the digital world and semiconductors, especially silicon, are at the base of each and every logic unit dealing in ‘ones’ and ‘zeros’. Some technological advances were triggered by fundamentally new effects such as the giant magneto-resistance (GMR) discovered in 1988. This is the basis for the standard hard-drives (HDD) as we know them. The HDDs however are already being replaced with so called solid state drives (SSD) which are based on flash memory. They owe their viability (cost, speed and storage density) almost entirely to the ability to produce a floating gate for a transistor on a scale down to tens of nanometers per single *bit* and while producing billions of  $\text{bits}/\text{cm}^2$ . There is thus a competition between shear ‘brute force’ miniaturization and the development of fundamentally new operation principles. This competition can be found in the “International Technology Roadmap for Semiconductors” which aims to guide the scaling of devices to follow “Moore’s Law” of improved performance and the white paper “Towards a “More-than-Moor” roadmap” which examines opportunities to include non-digital functionalities where performance don’t necessarily have to scale with size (both available at the ITRS website [rm15]). The competition between classical and quantum computing will be a particularly interesting example of this to follow in the near future.

## *1 Introduction*

As a side effect of miniaturization being a major factor in the improvement of all IT-hardware-technology, nanotechnology became somewhat of a buzzword. Fueled by this upwind for everything ‘nano’, a peculiar class of materials gained some academic interest: nanowires [XYS<sup>+</sup>03, LW07]. ‘Nanowire’ is a term used for many morphologies, but it seems a reasonable name for structures with a cross-section that is between  $1 \times 1$  and  $1000 \times 1000\text{ nm}^2$ , which are significantly longer than they are wide. One of the general aspects of this shape and also of nanostructured materials in general, is that the surface properties play a dominating role. This is simply caused by the fact, that there is a lot of surface per volume of material. The surface of non-fractal body scales with the characteristic length  $r$  as  $r^2$  while the volume follows  $r^3$ , therefore, the surface to volume ratio, proportional to  $1/r$ , gets very large for small structure sizes. Investigating nanowires as catalysts or sensing devices tries to take advantage of this large active surface area. The wire shape in particular has an inherent advantage here over three dimensionally constrained particles (nanoclusters, quantum dots etc.), in that it is easier to define contacts to and drive a current through a wire than through a point. The idea to combine this specific advantage of nanowires with new properties obtained by the stronger three dimensional confinement of quantum dots is the main idea behind the ‘Deutsche Forschungsgemeinschaft’ (DFG) project “wiring quantum dots” which funded this work.

Having somewhat motivated the use of semiconductor nanowires and before going into further detail on this specific project, first the “ion beam irradiation” part of the tile also needs an introduction. Although *Si* is the material of choice for microchips (hence “Silicon Valley”), as it is, pure silicon is a rather uninteresting material. The defining property of semiconductors is the ability to dramatically change their electronic properties by adding impurities [SN06]. As ion beam irradiation can be

used to ‘mix’ (i.e. dope) virtually any target material with a precisely controlled number of atoms of practically any element, it was and is a key part in the processing and development of semiconductor technologies. A specific example in which the combination of nanostructures and ion beams is advantageous is the ion irradiation of diamond to create nitrogen-vacancy clusters. These are interesting as promising components in a future quantum information device [BHK<sup>+</sup>10]. The precise control ion irradiation gives makes it possible to implant a well defined number of ions with reasonable spacial accuracy. This control is extravagantly demonstrated by the possibility of single ion irradiation [MVB<sup>+</sup>06, Ohd08].

In general, ion beam doping has the advantage over doping during the synthesis of nanostructures, in that it is not inherently limited by the chemical potentials and dynamics which typically have to be carefully controlled for the synthesis of nanostructures. It is a non-equilibrium physical process by which different elements can forcefully be introduced into a target matrix with much higher energies than those involved in chemical bonding. The extent of disorder created in the target during this bombardment, whether the intermixing is thermodynamically stable, and whether a desired (crystal) order can be reestablished by thermal annealing is in the focus of ion-beam physics. A good background on this can be gained from dedicated literature [ZLB85, Nas08, Sch12, Eck91].

Following these considerations, a further concurrence of nanotechnology and ion-irradiation is found in the search for a diluted magnetic semiconductor by implanting *Mn* in *GaAs* nanowires. As *GaAs* nanowires typically grow above 450°C but *MnAs* segregates from *Ga*<sub>(1-*x*)</sub>*Mn*<sub>*x*</sub>*As* at 350°C [DO06, SSK<sup>+</sup>11], there is no practicable way to dope *GaAs* with high concentrations of *Mn* during nanowire growth. The key insight was to do the irradiation at elevated temperatures, hot enough to minimize disorder, but cold enough to prevent segregation [BMB<sup>+</sup>11, PKB<sup>+</sup>12,

## 1 Introduction

Bor12, KPJ<sup>+</sup>13, PKJ<sup>+</sup>14]. In the before mentioned “wiring quantum dots” project such segregation was actually utilized to combine nanowires with nanoclusters. When *Si* nanowires are irradiated with high fluences of *Ga* and *As* and subsequently annealed with a flash-lamp, separated *GaAs* slices forme within the *Si* nanowires [PGL<sup>+</sup>14, Gla15]. The supersaturation of *Si* with *Ga* and *As* by ion implantation can thus be utilized to create *GaAs* – *Si* nanowire hetero-structures from a *Si* nanowire template in a relatively straight-forward manner.

A further example of the intersection of nanotechnology and ion beams is found in the ubiquitous focused-ion-beam (FIB) systems. The production and development of many of the novel applications of nanostructures on the horizon often requires the precise ion-beam milling that FIBs provide with a resolution of few nanometers. In all the examples given so far, and virtually per definition in the last one, typical structure sizes irradiated are in the order of magnitude of the irradiating ions. This warrants general investigations of the nanostructure - ion beam interaction [Bor12, GHB<sup>+</sup>13, NSUM14, JHMR15, UBNM15]. In the effort to understand principles and fundamental interactions on the nanometer length scales, nanowires are a very good model system to investigate as their geometry is fully characterized by their height and radius. Spheres, which would have a degree of freedom less, are unfortunately more difficult to handle, as the unavoidable proximity of a substrate may influence their behavior [Mö14, JHMR15]. Results obtained with nanowires are principally transferable to any nanostructure, however, this cannot of course be done in any general way explicitly, as the possible shapes are uncountable. This dissertation add to the growing field of nanostructure - ion beam interaction the discussion of three effects which are especially important in high fluence irradiation and dedicates a seperate chapter to each.

### Chapter 3 - Sputtering of Nanowires

In the dissertation of Dr. C. Borschel [Bor12] the program *iradina* [BR11] was developed and used to simulate the ion irradiation of nanostructures. It predicts an enhanced, diameter dependent sputter yield in nanoparticles. This chapter discussed the simulation and compares its predictions with experimentally obtained diameter dependent sputtering in nanowires. Some first results on the sputtering in the *Mn* irradiation of *GaAs* were obtained and published elsewhere [JNP<sup>+</sup>14]. The results presented here are on *Ar* irradiated *Si* nanowires. They were obtained in close cooperation with Stefan Noack in his M.Sc. and also published *publish*.

### Chapter 4 - High Doping Concentrations in Nanowires

The concentration of dopants does not follow a linear increase with the fluence of ions implanted for high fluences. It has already been observed in the early days of investigations into ion implantation that sputtering of the target will dynamically change its composition during the ion irradiation in addition to the intended change by incorporation of the ions within the target material [MEB88, Mö14]. This effect is enhanced in nanostructures, first since the sputtering is enhanced when compared to bulk samples as shown in the previous chapter, but also since there is simply less material in the structure. Hence, the effect of removing material by sputtering becomes significant at lower fluencies. The presented results are acquired by nano-XRF performed on 175 keV  $\text{Mn}^+$  ion irradiated ZnO nanowires [JNP<sup>+</sup>14]. They are discussed in comparison to a pseudo-dynamic simulation performed using results from *iradina*.

### Chapter 5 - Plastic Flow in Silicon Nanowires

In the high ion fluence irradiated *Si* nanowires a peculiar tendency

## *1 Introduction*

of the nanowires to become shorter was observed. This chapter presents a dedicated investigation into this plastic deformation of *Si* under ion irradiation which has been previously seen only in high energy ( $\geq MeV$ ) ion irradiations [Vol91, TR95, HKW04, HKW05].

## 2 Background

This chapter will provide a general scientific context for this dissertation. First a general outline of energetic ion-solid interaction is given. Then the possibilities of simulating this ion-solid interaction are discussed with an emphasis on those effects that will be relevant to the experiment in this thesis.

### 2.1 Ion-solid interaction

#### Energy loss

An energetic ion impinging on a solid will lose its kinetic energy to the solid in a variety of processes. The stopping power  $S$  is well described for a large energy range by the Bethe (sometimes “Bethe-Bloch”) formula derived using the Born approximation perturbation theory on the impact between the ‘fast’ ion and the ‘slow’ electrons in the solid:

$$S = \frac{dE}{dx} = -A \cdot \frac{\rho Z_2 \cdot Z_1^2}{\beta^2} \cdot \left[ \ln\left(\frac{B \cdot \beta^2}{Z_2 \cdot (1 - \beta^2)}\right) - \beta^2 \right], \quad (2.1)$$

with  $A$  and  $B$  positive combinations of constants,  $\rho$  the density and  $Z_2$  the atomic number of the target,  $Z_1$  and  $\beta = v/c$  the atomic number and relativistic velocity of the ion. Corrections to this formula are especially necessary for low ion energies, but in detail they are dependent on the

## 2 Background

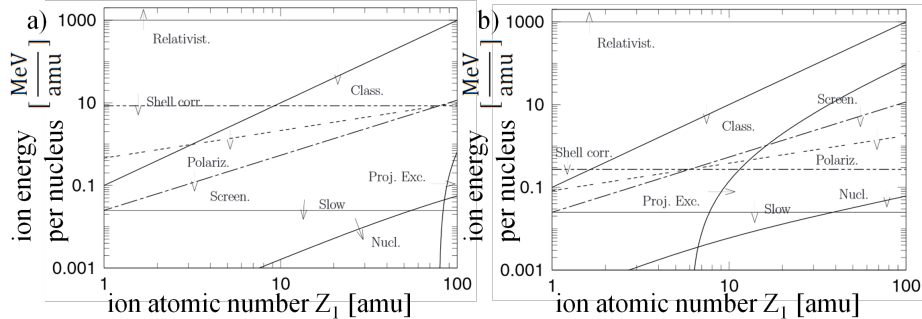


Figure 2.1: Illustration of the dominant effects on the stopping power for an ion of mass  $Z_1$  and energy  $E$  in  $Au$  a) and  $C$  b). Adapted from [Sig04].

target composition, the ion energy and ion mass in a non-trivial way. Figure 2.1 and the following discussion illustrates stopping regimes and why corrections are required to the Bethe formula. It is adapted from [Sig04].

At high ion energies ( $> 1 \text{ GeV}/\text{amu}$ , labeled “Relativist.”) highly relativistic effects have to be taken into account. At these energies we have, for example, Cherenkov radiation. Typically, nuclear reactions and resonances also occur at high ion energies. They may play a role at lower energies, especially for light ion-target combinations. However, as nuclear reactions may change the ion species, their cross sections are usually treated separately from the stopping power.

The horizontal line labeled “Shell corr.” marks the Thomas-Fermi velocity ( $Z_2^{2/3}v_0$ ) of the target electrons. The constant  $v_0 = e^2/\hbar = 25 \text{ keV}/\text{amu}$  is the Bohr velocity. In the parameter-space below this line the ion is moving at speeds comparable to that of the electrons in the target. In the low energy area below the line labeled “Slow” ( $25 \text{ keV}/\text{amu}$ ) the ion is traveling at speeds below the Bohr velocity of the target electrons. Here the ion velocity is only comparable to that of the valence electrons in the solid. Both these points mean that

## 2.1 Ion-solid interaction

the actual electron density distribution and chemical nature of the solid becomes relevant, which is of course not considered in the general Bethe formula. This makes a general and accurate theoretical prediction of electronic stopping impossible for low ion energies. Specific ion-target combinations require specific investigations.

Above the line showing the Thomas-Fermi velocity of the ion ( $v = Z_1^{2/3}v_0$ , “Screen.”) the ion can be assumed to be stripped of all its electrons. Below, a screening function must consider the effective charge of the ion. Below the curve labeled “Proj. Ext.” the ion (projectile) carries a comparable number of electrons to the target making excitation processes in the electronic configuration of the ion significant.

For ion velocities  $v < (Z_1 Z_2)^{1/3} v_0$  (labeled “Polariz.”) a higher order ( $Z_1^3$ ) correction term to the Bethe formula becomes relevant due to the Barkas-Andersen effect. Below the line marked “Class.” ( $Z_1^2 \cdot 100 \text{ keV/amu}$ ) classical Bohr orbits can be used for electrons around the ion, this is a *sufficient* criterion for the derivation of the Bethe formula not a *necessary* one.

Finally, not be confused with the nuclear reactions already mentioned, in the region marked “Nucl.”, at low ion energies and for large ions, the interaction with the electronic system becomes weak. Here the contribution of the coulomb interaction between ion and individual target atoms as a whole become the main contribution to slowing the ion. This is called nuclear stopping in contrast to the electronic stopping discussed so far, as kinetic energy is transferred to the target nuclei, not just the electrons.

Those ion-solid interaction processes which are specific to the properties of the target material can be used to characterize it. These methods are summarized as ion beam analysis (IBA). A confident and comprehensive review of the possibilities of IBA can be found in reference [JBB<sup>+</sup>12].

## 2 Background

The effects that the ion irradiation has on the solid will be discussed next by looking at the electronic and nuclear energy loss separately.

### Discussion of electronic energy loss

Electronic stopping  $S_e$  “excites the electronic system”. In the simplest case a target atom is ionized, followed by a host of effects such as characteristic X-ray emission and Auger electron emission associated with the relaxation of this excited state. Analogously, excitation in a semiconductor is associated with band to band, exciton etc. recombination. Detection of these emissions can be used for IBA. The luminescent and fluorescent relaxation mechanisms are, however, generally not very efficient. Most of the energy deposited in the electronic system will be turned into kinetic energy of electrons and subsequently converted to heat. This happens very locally on the  $nm$  scale of the electrons mean free path and thus also very quickly, within the order of  $ps$ .

The effects of such local heating on a solid are diverse. Defects and amorphous regions may either appear or disappear, depending on the material and its history. For large ion masses and energies (swift, heavy ions), the deposited energy density becomes large enough to form an “ion track” around the path of the ion. Ion tracks are a whole field of research outlined well by references [TDP92, MK97, WKW04]. Very large electronic losses have to be treated carefully as a large percentage of the electrons within the track are energized and some electrons also gain a significant amount of kinetic energy.

The energies used in this dissertation are in the order of  $\approx 100\text{ keV}$  with elements of mass  $\approx 100\text{ amu}$ . The energy regime investigated in this dissertation is thus right at the bottom of the area plotted in figure 2.1. Electronic stopping is not dominant, so that it is sufficient to treat the electronic energy loss as a local heat source.

## 2.1 Ion-solid interaction

### Discussion of nuclear energy loss

The seemingly more straightforward process in the energetic ion-solid interaction is an elastic collision between the impinging ion and a target atom. Its first observation was in the famous Rutherford (Geiger–Marsden) experiment [Rut11] which was groundbreaking to understanding the structure of matter. Nuclear energy loss is caused by the kinetic energy which is transferred from the energetic ion onto an atom in the target. An impinging ion can transfer considerable energy to an atom, which in turn will collide with other lattice atoms, leading to the formation of a collision cascade. This displacement of atoms from their lattice position is the main contribution to irradiation damage and sputtering of the target.

The amorphization of crystalline semiconductors has been investigated extensively with a good review found in reference [WWS12]. The damage production depends a lot on the irradiated semi-conductor and on the density of the collision cascade caused by the irradiating ion. In general the defects produced by nuclear energy loss are Frenkel pairs. On further irradiation, the Frenkel pairs can agglomerate to form extended defect clusters which initiate amorphization. The fluence at which the material is amorphized is highly temperature dependent as Frenkel pairs can anneal at high implantation temperatures. This can lead to an arbitrarily high amorphization fluence, if the annealing of defects is faster than their creation. A typical ‘radiation hard’ material is  $ZnO$  which is not amorphous even after  $10^{17} \text{ cm}^{-2}$  of  $200 \text{ keV Ar}^+$  irradiation at  $15 \text{ K}$  [WWS12]. An arbitrarily large amorphization threshold can also be obtained for  $Si$  irradiated with  $300 \text{ keV Ar}^+$  at  $300^\circ \text{ C}$  ( $\approx 600 \text{ K}$ ) [PMB04].

In addition to the activation of defect recombination by increasing the ‘global’ temperature, an increased local temperature by the energy deposited by the ion will also lead to ‘dynamic annealing’. In a recent study

## 2 Background

[TVM<sup>+</sup>15] the dynamic annealing was enhanced by the simultaneous irradiation with  $36 \text{ MeV} W$  a swift, heavy ion leading to predominantly electronic energy loss and  $900 \text{ keV} I$  leading to large nuclear losses. Simultaneous irradiation lead to much less damage in the irradiated *SiC* than subsequent irradiation. The reduction of structure sizes also leads to larger dynamic annealing as there is less material into which the energy deposited by the ion can dissipate, leading to higher local temperatures. This was shown in the *Mn* irradiation of *GaAs* nanowires [Bor12, JHMR15] and could be used to improve the magnetic properties of the *GaAs : Mn* nanowires [BMB<sup>+</sup>11, PKB<sup>+</sup>12, KPJ<sup>+</sup>13, PKJ<sup>+</sup>14].

A typical assumption in the theoretical treatment of nuclear energy loss is the binary collision approximation (BCA) for the ion and the target atoms. Under this assumption nuclear stopping is treated as a series of collisions between single particles. With the additional assumptions of 1) a spherically symmetric interaction potential and 2) the neglect of possible electronic effects (chemical binding) between the collision partners, the angular-momentum is conserved in the collision and the classical scattering-integrals can be solved.

The resulting trajectories of a *Si – Si* collision at  $10 \text{ eV}$  is plotted in figure 2.2. The large difference between the Moliére screened Coulomb potential and the *Si – Si* potential derived by Dirac-Fock-Slater code is clearly visible. The former is a purely repulsive Coulomb interaction, while the latter includes an attractive interaction for large interatomic distances similar to the well known Lennard-Jones potential [Eck91]. For high energy collisions a “universal” ZBL potential based on Coulomb interaction is quite successful [ZLB85], however for low energy collisions a generalized formula cannot be accurate and specific potentials have to be developed for each combination of collision partners [Ded95, NRS97, ANNK02, ND08].

## 2.1 Ion-solid interaction

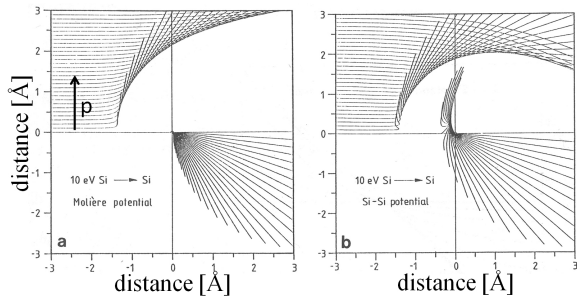


Figure 2.2: Trajectories of a 10 eV  $Si - Si$  collision for a) Moli  re and b)  $Si - Si$  potential. The trajectories end after the same elapsed time for each impact parameter  $p$ . Adapted from [Eck91].

In addition to this problem of finding the correct interaction potential for a collision, depending on the ion and the atomic structure of the irradiated material, the collision parameters relevant to low energy collisions are within the order of the inter-atomic distance of a few Å, see figure 2.2. The assumption that this is still a binary collisions can no longer be valid. In conclusion, it has to be noted that similar to the electronic stopping case, the assumptions for a generalized treatment of nuclear stopping are well fulfilled for large ion energies, but lose their validity at low energies  $\ll 1 \text{ keV}$ .

### Sigmund theory of sputtering

A prominent role in this dissertation will be played by a special effect of nuclear energy loss arising when the path of a recoiled atom intersects the targets surface: sputtering. The foundation of sputter theory was laid by Sigmund [Sig69]. It is outlined in the following. The nuclear stopping of ions leads to the formation of highly branched collision cascades and most of recoiled atoms are found at the end of the many branches. Because of this, the majority of sputtered particles has a low energy and thus a low range in the material [Tho68]. They must thus originate from the surface

## *2 Background*

of the target and the sputter yield, as the number of atoms sputtered per impinging ion, can be estimated by calculating the nuclear energy loss at the surface of the irradiated material and dividing it by a factor to account for the probability of an atom leaving the solid.

The probability for the atom to leave the solid includes geometric considerations and the ‘surface binding energy’ (SBE). A possible model for an atom leaving a solid is that of a potential plateau with the height of the enthalpy of sublimation which has to be overcome by the atom approaching the surface. This equates the energy required for sputtering an atom to the thermal energy required for sublimation. For metals this is a good assumption, as the metallic bond is undirected and mediated by the electron gas. However, the SBE model for sputtering neglects all effects related to the directionality of the local binding forces experienced by the atom to be sputtered and the modification of the surface by repeated removal of atoms, which will be relevant in compounds with covalent and ionic bonds.

A reasonable assumption for the mean nuclear energy deposition distribution is a Gaussian ellipsoid, with the center at the ion range and the longitudinal and lateral straggling naturally defining its extensions. This approach was used by Sigmund to arrive at a good explanation for the energy dependence of sputtering from flat surfaces. Starting at low energies, the sputter yield will initially increase with increasing energy, simply due to more energy being available. For further increasing energy, however, the ion range becomes larger, leading to a predominant deposition of the energy deeper inside the target, away from the surface. A maximum is thus found at energies where the ion range is in the order of the longitudinal straggling. The angle dependence of sputtering can also be explained by the increased deposition of energy near the surface for larger angles of incidence, as shown in figure 2.3.

## 2.1 Ion-solid interaction

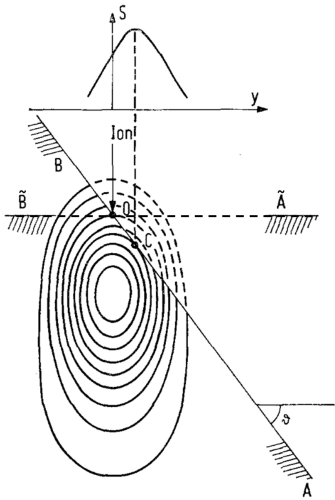


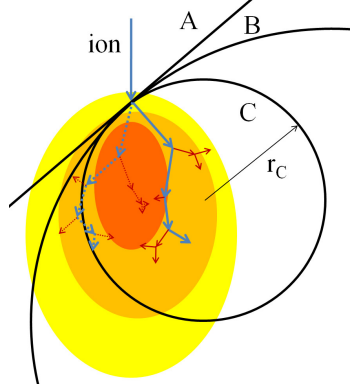
Figure 2.3: Illustration of the Sigmund model of sputtering for irradiation of a bulk sample at an angle  $\theta$ . The ion enters the target at the point O and deposits the nuclear energy as indicated by the oval contours. The energy deposited along the inclined surface BA is larger than that for the perpendicular surface BA leading to increased sputtering for irradiation at an angle. Also the deposited energy and thus sputtering is not largest exactly at the point of incidence O, but further down at the point C. This is illustrated by the projection of the sputter yield ‘S’ onto the lateral dimension ‘y’. Adapted from [Sig73].

The Sigmund theory can also been applied to more complex surfaces. The Bradley-Harper theory of ripple formation on ion irradiated planes relies on the anisotropic sputtering predicted by the Sigmund model applied to a structured surface [Sig73, BH88]. The increased sputtering at a point (C) downstream from the point where the ion enters the target (O) leads to an enhancement of surface roughness.

The Sigmund theory predicts a maximum in sputtering where the ion range is comparable to the nanostructure diameter. This can be understood by considering sputtering for a fixed ion energy and varying diameter, illustrated in figure 2.4. At large diameters atoms can only be sputtered from the surface facing the ion beam. The sputter yield will still be larger than for a bulk sample as the local angle of irradiation is increased for non central impacts (A in figure 2.4). For decreasing diameters the curvature of the wires increases, further increasing the intersection area between the estimated energy distribution and the nanowire (B in figure 2.4). Once the diameter is in the order of the ion range, ‘forward’ sputtering along the direction of the ions initial path will become possible (C in figure 2.4). There is a maximum sputter yield for a radius

## 2 Background

Figure 2.4: Illustration of the Sigmund model of sputtering for irradiation of a curved surface. For an infinite curvature radius (straight line A) a non-central impact is the same as irradiation at an angle, as shown in figure 2.3. For decreasing radii (B) the intersection between the colored energy distribution and the surface is increased. For small radii ( $r_C$ , C) forward sputtering appears. Two exemplary ion paths contributing to the colored average energy distribution are shown. The dashed path leaves and returns to the the smallest structure C.



comparable to the ion range, as the total surface area shrinks as  $1/r^2$ , reducing the sputter yield again for decreasing diameters.

This model is obviously limited, as the nuclear energy distribution is assumed to remain constant even if the target surface intersects it (dashed lines in figure 2.3). The maximum in the Gaussian ellipsoid approximation of the mean nuclear energy deposition is found where many of the branches of collision cascades overlap. A constant distribution wrongly includes those ion paths that would have left the nanostructure, as shown by the dashed ion trajectory in figure 2.4. The more detailed description of the process thus required is outlined in the following section on the simulation of ion-solid interaction.

## 2.2 Simulation of ion-solid interaction

In practice, the theory of ion-solid interaction is implemented in simulation tools which allow the experimenter to predict experimental outcomes. Most frequently the energy dependence of the ion range is obtained by simulations and used to decide which energy and fluence of

## 2.2 Simulation of ion-solid interaction

irradiation is needed to create a desired doping concentration profile. On a more fundamental level, an experimentally observed behavior can be understood better by comparing it to various simulations to discern the dominating effects. The two main simulation approaches used to simulate the ion solid interaction are Monte-Carlo (MC) and Molecular Dynamic simulations (MD), both outlined in the following sections.

### Monte-Carlo and the binary collision approximation

Monte-Carlo codes are simulation codes that use random numbers for simulations. After numerous simulations with different randomized outcomes, a statistical approximation of the likely outcome can be derived. With the BCA, the solid ion-interaction lends itself very well to MC simulation, as the evolution of a collision cascade can be simulated by following the paths of the ion and all recoils re-iteratively from one collision event to the next. The probability of a collision can be determined from the cross-sections determined by the interaction potential between the projectile and the atoms in the target. According to this probability, a randomized distance traveled in a straight line by the projectile is determined. The particle's kinetic energy is reduced by the electronic energy loss accordingly. This has the underlying assumption of a ‘random material’ and crystal structure effects such as channeling are not reproduced by such a simulation. Two further random numbers are used to determine the impact parameter and azimuthal angle. The trajectories of the projectile and target atom in the plane of impact after the impact are determined by this impact parameter, the interaction potential and the particle energy, as shown in chapter 2.1, figure 2.2.

Examples of simulation codes implementing this approach in planar targets are TRIDYN [ME84], SDTrimSP [BMS<sup>+</sup>08], cordeo [Sch08], COSIPO [Hau84] and, by far the most popular, SRIM [Zie12]. In TRIDYN and

## 2 Background

SDTrimSP the target composition can be ‘dynamic’, changing with the incorporation of ions and with selective sputtering of target atoms and the incorporated ions. It is clear from the discussion of chapter 2.1, figure 2.4 that the irradiation of a nanostructure can not be approximated well with a planar simulation. Therefore, the recently developed TRI3DYN [Mö14] and *iradina* [BR11] run a BCA MC simulation in a volume subdivided into rectangular voxels containing either vacuum or material to represent a three dimensional, structured target. TRI3DYN even includes dynamic composition and structural relaxation during the irradiation on a three dimensional simulation volume, but unfortunately it is not publicly available yet. Several *iradina* simulation results will be discussed in this thesis, so the following points on the expected accuracy have to be made.

The strong point of MC BCA simulations in general is that the direct simulation of the ion trajectories gives an accurate prediction of the final distribution of the ions in the target. This is a result of the sufficient accuracy of the previously discussed underlying theory of the energy losses for high energies. These predominantly determine the distance traveled by the ion in a collision cascade and also the distribution of nuclear and electronic energy loss. As the simulation directly follows the ions path, this accuracy can be expected to be upheld in the irradiation of nanowires. The concentration of incorporated ions is somewhat lower in nanowires than in bulk targets, as in a nanowire there are more possible paths that lead to the ions being scattered out of the nanowire, than there are in the irradiation of a bulk surface, see chapter 2.1, figure 2.4 and reference [Bor12].

Predicting the damage caused in the material by nuclear energy loss is a much more difficult prospect. The *iradina* code checks at each collision whether the target atom acquires more energy than the “displacement energy” which is a material specific parameter. If an atom has less

## 2.2 Simulation of ion-solid interaction

than the displacement energy after a collision, it is assumed to remain bound in its place and the energy is converted into lattice vibrations (= heat). Atoms with more energy are displaced, creating a Frenkel pair which is counted as an interstitial at the location where the atom finally comes to rest and a vacancy at its point of origin. The displacement energy is experimentally accessible for crystalline materials by electron irradiation experiments in which the irradiating electron energy is in the order of *MeV*. From the electrons' impulse and mass the maximum transferred energy can be calculated. The defects produced as a function of electron energy can thus be used to determine a threshold energy for point defects, and this value is defined as the displacement energy. This is not possible for amorphous materials, where point defects are ill-defined. Also, the number of Frenkel pairs this simulation creates is only an estimation at the *creation rate* of the defects. The critical role that defect mobility, agglomeration and annealing plays in irradiation damage is totally neglected [Nor14].

Better results can be expected for the computation of sputtering, for which an excellent review is given in reference [Bie87]. The difficulty is that for low projectile energies the interaction with both the nuclear and the electronic system are not generalizable, as discussed in chapter 2.1. This is a problem, as the dominating contribution to sputtering is made by low energy recoils [Tho68]. The various relevant interaction potentials however differ most at low energies. In addition, the SBE model used for Sigmund sputtering is just an approximation of the complexities arising at real surfaces. For metals the situation is most favorable and in reference [Bie87] sputter yields of various metals are reproduced quantitatively. More recently, in reference [HZM14] by Hofsäss et al., good results on the sputtering of *Si* and *Ge* were obtained using the *Kr – C* [WHB77] potential which was found to be superior to the ZBL potential [ZLB85]. Only the ZBL potential is implemented in *iradina*,

## 2 Background

however, neither the  $Kr - C$  nor the ZBL potential reproduce the angle dependent potential covalently bonded solids such as *Si* [SW85, Ter88]. Radially symmetric potentials are always only an approximation and which potential provides the better approximation in which scenario is not generally clear.

Hofsäss et al. also report a change in the dependence of sputtering on the angle of incidence for different interaction potentials. This might be worrisome even for the qualitative dependencies in the irradiation of nanostructures investigated in this thesis. However, the effect on sputtering is caused by the change in the critical angle for scattering at the surface of the impinging ion, not by a later change in the distribution of the nuclear energy deposition within the target. Since the critical grazing incidence angle is close to  $0^\circ$  regardless of the interaction potential for the relatively high energies ( $\approx 100\text{ keV}$ ) used in this dissertation [YS84], the accuracy of qualitative predictions will be unaffected. Finally, Hofsäss et al. also investigated the compounds  $Ta_2O_5$  and  $SiO_2$  finding that dynamic simulations are necessary, as preferential sputtering and composition changes play a significant role. This is not possible in *iradina* and will be discussed where relevant.

Even though *iradina* can implement an analytical description of a cylinder, most of the simulations in this work were nevertheless performed on the voxel based simulation volume, as this granted more freedom in the creation of the simulation volumes. Where the axial distribution was not relevant, the voxel  $z$ -size was set to  $10\text{ nm}$  with periodic boundary conditions. The accuracy of the approximation of a curved surface in the  $xy$  direction, such as the surface of the cylindrical nanowires, is obviously dependent on the voxel size. Since the surface of the approximation by rectangular voxels of a cylinder is strictly larger than the analytical surface, sputtering may be slightly increased. Also, the possible ions' impact angles are limited to the angle between the ion

## 2.2 Simulation of ion-solid interaction

beam and the plane surfaces of the voxels facing the ion beam, so that the impinging angle is always larger in the voxelated surface than for the analytical surface. This will have no large effect, since, as before, the small critical angles for reflection of ions are restricted to the very outermost edges of the nanowire. Considering these effects, it was found that for voxel edges of  $2\text{ nm}$  and below only a negligible influence of the voxel size on the sputtering remained. In summary, the prediction of sputtering as simulated by *iradina* in this thesis is expected to be dependable with respect to the qualitative relationship between ion range and structure size, and sputtering, while quantitative sputter yields will be inaccurate.

### Molecular dynamic simulations

The MC BCA simulations outlined so far inherently neglect all effects occurring when more than two particles move at the same time. Molecular dynamic (MD) simulations, however, follow the path of every particle in the simulation volume individually, calculating the interaction potential between them at every time step [AW59]. Obviously this is much more computationally expensive than the BCA and simulation volumes and times are thus limited. Nevertheless the method can be applied to ion irradiation [Nor95] and increasing computer power has led to the simulation of ever higher particle energies, which require a larger simulation volume and time [GHB<sup>+</sup>13, BD14, ABU15]. The interactions between the target atoms in the MD simulations have to recreate the atomic structure, thermal vibrations etc., so that the low energy regime of the interaction potential is critical and has to be adapted to the specific problem [Ded95, NRS97, ANNK02, ND08]. Electronic energy loss can be included as a frictional force, however, treating this energy in a consistent manner is a problem, as the electronic system is typically not

## *2 Background*

explicitly represented. Since MD simulations can reproduce the thermal evolution of a system, references to relevant MD simulation studies will be included in the discussion of results in this thesis.

### **Relevant simulations in literature**

Two recent investigations on sputtering of spherical [NSUM14] and cylindrical [UBNM15] nanostructures have to be mentioned here as they overlap significantly with the studies made in this thesis. These publications have found the Sigmund model to be a decent first approximation for sputtering as it was discussed in chapter 2.1. They go on to compare the sputter yield results from MC and MD simulations and discuss its diameter dependence. Unfortunately, the nanowire diameters investigated by MD are quite small owing to the computational costs. They find that for decreasing nanostructure diameters sputtering of clusters and thermal evaporation become increasingly important due to the lower number of atoms amongst which the ion deposited energy is distributed. This dissertation adds to results of these studies with simulations of diameter and energy dependent sputtering of nanowires in chapter 4.2 and an experimental investigation of this dependency in the following chapter 4.4.

# 3 Experimental Methods

## 3.1 Nanowire synthesis

Nanowire synthesis can be categorized according to two approaches: “bottom-up” and “top-down”. The “bottom-up” approach relies on the self-organized arrangement of matter using an inherent anisotropy in the growth mechanism to create nanoscale structures. Depending on the material, crystal quality, morphology, infrastructural requirements, the quantity to be produced etc. there is a large variety of processes available for synthesis. The *ZnO* [BMS<sup>+</sup>06, Sti08, Mü09, Ogr13], *GaAs* [BDSS04, WDJ<sup>+</sup>09] and *Si* [LSH<sup>+</sup>08] nanowires investigated in this dissertation were grown using vapor transport, MOVPE and chemical vapor deposition respectively.

A very common mechanism to create the anisotropy required to get the one dimensional growth of nanowires is the vapor-liquid-solid growth (VLS) first described by Wagner and Ellis [WE64]. The variety of processes listed before are responsible to provide the ‘vapor’ of material for this growth mechanism. With the vapor transport technique the source material eg. *ZnO* is simply evaporated in a typically inert atmosphere and transported within a reactor to the substrate by diffusion or gas flow. Chemical vapor deposition uses reactive gases such as *SiH<sub>4</sub>* to provide the source material, in this case *Si* in a temperature and pressure controlled reactor. Similarly in MOVPE a metal-organic gas is used as at

### 3 Experimental Methods

least one of the sources, for example TMG (trimethylgallium) and  $AsH_3$  to grow  $GaAs$ .

Although self-catalyzed growth has also been observed, the liquid part exploited in VLS is typically provided by a metal catalyst deposited on the growth substrate. The material in the vapor phase can accumulate in the catalyst droplet until the concentration is supersaturated. Preferential segregation of the excess material at the droplet-substrate interface leads to the growth of a nanowire. The size of the droplet can be used to control the diameter of the grown nanowire to some extent. The growth of the “bottom-up” nanowires used in this thesis relies on the VLS mechanism. An epitaxial relation between the substrate and the nanowire material may be used to direct the growth. Typical nanowire diameters and lengths are  $50 - 300\text{ nm}$  and  $> 5\text{ }\mu\text{m}$  respectively.

Nanowires can also be synthesized “top-down”. A “top-down” approach requires a predefined template which is used to control the desired morphology. The  $Si$ -nanowire arrays used to study sputtering and plastic deformation within this dissertation were etched by reactive ion etching (RIE) through a circular, e-beam lithographically defined  $Ni$  hard-mask which set the nanowire diameter [JNW<sup>+15</sup>]. Using the “top-down” etching process it is possible to prepare nanowires with diameters varying from  $50\text{ nm}$  to  $2\text{ }\mu\text{m}$  with a height of  $\approx 3\mu\text{m}$  on a single substrate for simultaneous irradiation. The spacing between the nanowires was set to larger than their height, so that there is no shadowing of the ion beam between the nanowires.

Since the growth of nanowires was performed mainly by collaborators in Lund University ( $GaAs$ ) and TU Vienna ( $Si$ ) and is not part of the investigations reported here, the inclined reader is redirected to the cited references for further details respective growth parameters and their determination.

## 3.2 Modification

### ROMEO

The ion irradiation for this dissertation was performed at the general purpose High Voltage Engineering implanter “ROMEO” at the IFK in Jena. It can provide an ion beam of virtually any element at energies ranging from  $10 - 380 \text{ keV}$ . The beam passes a  $90^\circ$  selector magnet and can be swept with a frequency of  $\approx 1 \text{ kHz}$  to homogeneously irradiate areas up to several tens of  $\text{cm}^2$  with ion currents of up to  $1 \text{ mA}$ . For this work ion current densities were limited to  $500 \text{ nA/cm}^2$ , corresponding to  $\approx 15 \text{ min}$  for the typical fluence of  $10^{16} \text{ ions/cm}^2$ .

As a previous work has shown that nanowires can bend under ion irradiation [BSL<sup>+</sup>11, Bor12], a rotatable and heatable, tilted stage (RHT) was custom built [Noa14]. With it, bending of the upstanding nanowires can be avoided as they are irradiated homogeneously from all sides at an angle of  $45^\circ$ . All the samples investigated in this thesis were rotated on the RHT and its preceding prototype sample stages during the irradiation.

The sputtering and plastic deformation studies in chapters 4.4 and 6.2 were conducted with  $\text{Ar}^+$  irradiation in  $\text{Si}$  nanowires to avoid any chemical effects of the incorporated ions. To prevent defect induced density changes and the  $\text{Si}$  nanowires from amorphizing, the irradiation temperature was  $300^\circ$  for the sputtering study. At this temperature the amorphization threshold becomes arbitrarily high [PMB04]. The other irradiations were performed at room-temperature. For the quantification of dopants  $\text{ZnO}$ -nanowires were irradiated with  $\text{Mn}^+$ . First  $\text{Mn}$  has a similar mass to  $\text{Zn}$  and both are medium-weight so that the linear cascade theory is applicable. Also,  $\text{ZnO} : \text{Mn}$  is interesting as a possible material for diluted magnetic semiconductors (DMS) [Fur88, NKA<sup>+</sup>04]. Pragmat-

### *3 Experimental Methods*

ically, it is relatively easy to get a stable  $Mn^+$  beam with ROMEO and with the quantification in mind,  $Mn$  is much less likely to be in any components and give a background than  $Fe, Co, Ni$  or  $Cu$ .

#### **Focussed ion beam - FIB**

Some sample preparations required a FIB. They are highly specialized ion accelerators with the main objective of obtaining a small ion beam focus. Most of the systems use a  $Ga^+$  beam and acceleration voltages up to  $30\text{ keV}$ . The main use for FIBs is to sputter material extremely locally, making it a versatile tool for nano-machining. The FEI DualBeam Helios NanoLab 600i FIB system used for this dissertation is a scanning electron microscope (SEM) - FIB combination. The sample can thus be milled with the ion beam and investigated with the SEM re-iteratively. The system is also equipped with a  $Pt$ -metal-organic gas injection system. The  $Pt$  containing organic molecule can be cracked locally on the sample by the secondary electrons created by either the electron or the ion beam. The FIB system can thus mill and deposit structures on a  $nm$  scale. For the sample preparation in this thesis all  $Pt$  deposition was done with the electron beam. Most of the  $Pt$  is deposited near the impact point of the primary beam at the substrate. However, typically a rather large ‘halo’ of minor  $Pt$  deposition can extend for a couple of  $\mu m$ .

## **3.3 Characterization**

#### **Scanning Electron Microscope - SEM**

The morphological changes in the nanowires were characterized by high resolution SEM in the FEI DualBeam Helios NanoLab 600i FIB system. The spacial resolution of the SEM system is  $\approx 2\text{ nm}$ . Images of individual nanowires were made before and after ion irradiation, to quantify

### 3.3 Characterization

the sputtering. To find exactly the same place on the sample, a series of images with increasing magnification has to be made. Typically, images were made at an angle of  $45^\circ$  to the substrate with the alignment procedure the same before and after irradiation.

A semi-automated image analysis protocol was developed by Stefan Noack in his Master thesis [Noa14, ?] to evaluate the SEM images of a large number of nanowires. It applies a (3x3) median filter to smooth out some noise and a Gaussian unsharp mask with  $\sigma = 1\text{ px}$  and weighted at 60 % to resharpen the edges [San04]. An Otsu threshold [Ots79] is applied to separate the brighter nanowire from the darker background. Next, open source particle analysis software is used to find the main body of the nanowire and turn it upright, correcting any marginal tilt remaining in the SEM images [SACF<sup>+</sup>12, SPTS12]. Finally the sum of the gray-values in each line used to calculate the diameter at that height along the nanowire axis. As the investigated nanowires showed a characteristic bulge at the base, this point was used to align the height profiles of a single wire before and after irradiation. To avoid any irregular effects by the altered geometry at the top facet and the base of the nanowire,  $\approx 20\%$  of the height was disregarded at either end of the extracted profile. After a fluence of  $10^{16}\text{ cm}^{-2}$  the change in diameter was close to the resolution limit of the SEM, therefore only the data for subsequent irradiation steps of  $2 \cdot 10^{16}\text{ cm}^{-2}$  ions was evaluated. A more detailed description of the image analysis process can be found in [Noa14] and the supplementary information of reference [?].

### Electron Back-Scatter Diffraction -EBSD

A Carl Zeiss Auriga CrossBeam Workstation fitted with a EBSD tool was used to identify whether nanowires remained crystalline after irradiation. The electron beam is focused on the sample at an arbitrary

### *3 Experimental Methods*

angle and the scattered electrons are detected by a large CCD detector in the SEM. Bragg diffraction along the crystal lattice planes produces a characteristic pattern of Kikuchi lines on the detector [Kik28, FH13] in crystalline samples. Amorphous or nano-crystalline samples show no pattern.

#### **nano-XRF**

The experimentally most advanced characterization method was X-ray fluorescence with a nano-focussed X-ray beam (nano-XRF) at the European Synchrotron Radiation Facility (ESRF), beamlines ID16b and ID13. Hard X-ray radiation stimulates the atoms within the radiated material to emit characteristic X-ray radiation. This X-ray fluorescence can be detected in an energy dispersive semiconductor detector and used to identify and quantify the elements in the sample. In principle the method is similar to the more wide-spread energy dispersive X-ray spectroscopy (EDX), where an electron beam is used to excite characteristic X-ray fluorescence. Very good lateral resolution can be obtained by having an EDX detector in a SEM. The advantage of using X-rays lies in the absence of Bremsstrahlung which high energy electrons produce in matter in addition to characteristic X-rays. In XRF there is thus a much lower background and much lower concentrations of elements can be detected and quantified. Unlike normal X-ray tubes, synchrotron radiation is very brilliant, allowing it to be focused. The beamlines ID16b and ID13 were run at various energies above 16 keV and with focal spot of typically  $\approx 80\text{ nm}$  and  $\approx 250\text{ nm}$  diameter respectively. The nano-XRF thus allows the quantification of low concentrations with sufficient lateral resolution to resolve axial concentration gradients in a nanowire. Unfortunately, the resolution is not high enough to investigate radial distributions.

### 3.3 Characterization

At both beamlines the nanowires are scanned under the fixed focal point of the X-ray beam with piezo-motors, while the XRF spectra are collected with a Vortex EM silicon drift X-ray detector. For this thesis, *Mn* irradiated *ZnO* nanowires were deposited on TEM grids either randomly by ‘imprinting’ or individually by using the micro-manipulator in the FEI DualBeam FIB. Transferring individual wires requires some finesse, but it is possible to detach *ZnO* nanowires from their substrate without the  $Ga^+$  FIB and to place them on the “lacey-carbon” TEM grids without any additional *Pt* deposition. In this way SEM images before and after irradiation of the same wire investigated by nano-XRF are available.

The spectra used for quantification were obtained in multiple scans across a nanowire at regular intervals along its length. As the XRF signal can be used to locate the nanowire, only the points near the nanowire were measured with a high integration time and a low step-with ( $< \frac{1}{2}$  focal spot) to ensure a large number of counts ( $> 10^5$  per scan) at reasonable measuring times.

#### nano-XRF quantification

The XRF-Spectra were evaluated using the open source PyMCA software package [SPC<sup>+07</sup>]. The effects of self absorption and excitation can be neglected, as the investigated nanowires are very thin compared to the X-ray absorption length, which is a couple of  $\mu m$  in *ZnO*. However, the detector-sample distance is responsible for an unavoidable attenuation length in air. Here the X-ray absorption is dominated by *Ar*. As *Mn* is relatively light, its characteristic X-ray emission at  $K_{\alpha,Mn} = 5.9 \text{ keV}$  is absorbed more than the signal of the heavier *Zn* with  $K_{\alpha,Zn} = 8.6 \text{ keV}$ . Thus, absorption of the XRF signal in air has to be considered carefully in the fitting with PyMCA. The accuracy was double checked by mea-

### 3 Experimental Methods

suring and quantifying trace elements in a calibration sample of bovine liver. In this way optimal fitting parameters were found for each beamtime and applied to the respective spectra in the PyMCA batch mode. Oxygen cannot be quantified in these beamlines, as its XRF emission is totally attenuated by air and a *Si* dead layer in the detector. The quantification of the *Mn* content in the *ZnO* nanowires thus relies on the assessment of the *Mn/Zn* ratio. It is a decent approximation to assume that the *ZnO* remains stoichiometric even during the irradiation. The samples are irradiated in a chamber with a base pressure  $\approx 10^{-6}$  mbar, so according to the Hertz-Knudsen equation this will give a coverage of roughly one mono-layer or  $10^{15}$  particles/cm<sup>2</sup>s. The maximum ion current density yields  $10^{13}$  ions/cm<sup>2</sup>s, so that an unlikely amount of preferential sputtering would be required to deplete the oxygen out of the wires. In any case, the wires will be oxidized in the normal atmosphere post irradiation. The *Mn/Zn* ratio is thus a good proxy for the *Mn* concentration.

The quantification limit can be estimated within PyMCA. By finding an appropriate photon flux and nanowire interaction volume a simulation can reproduce the XRF spectrum with the actually measured number of counts at  $K_{\alpha,Zn}$ . The *Mn* content in the simulated matrix can then be decreased until the minimum *Mn* content is found which gives a signal at  $K_{\alpha,Mn}$  just above the actually measured noise level. In this way a lower limit for the concentration resolution can be found at typically 0.1 % *Mn/Zn*.

# 4 Sputtering of Nanowires

This chapter will investigate the sputtering of nanowires. The experiments were conducted together with Stefan Noack and are partially published in his master thesis [Noa14] and in Nano Letters [JNW<sup>+</sup>15].

## 4.1 First results in $Mn$ irradiated $GaAs$

Introduction by Mn in GaAs (JPhysD)

## 4.2 Simulation results

A good understanding of the sputtering of nanowires can be gained by looking at MC simulations results performed with *iradina*. From the discussion of the Sigmund sputter model in chapter 2.1 a maximum is expected for a certain ion, ion energy and nanowire diameter combination. This is confirmed by MC simulations shown in figure 4.1a and 4.1b for the examples of  $Xe^+$  and  $Ar^+$  ions, respectively, irradiating a nanowire at an angle of  $45^\circ$  to the nanowire. Note that the color profile is not identical as sputtering is about a factor of  $2,5 \times$  larger for the denser collision cascades caused by the heavier  $Xe$ .

For both irradiations a black line indicates the ion range calculated with SRIM and projected on to  $45^\circ$ . The maximum of the sputtering correlates very well with the ion range. This can also be seen in 4.1c,

#### 4 Sputtering of Nanowires

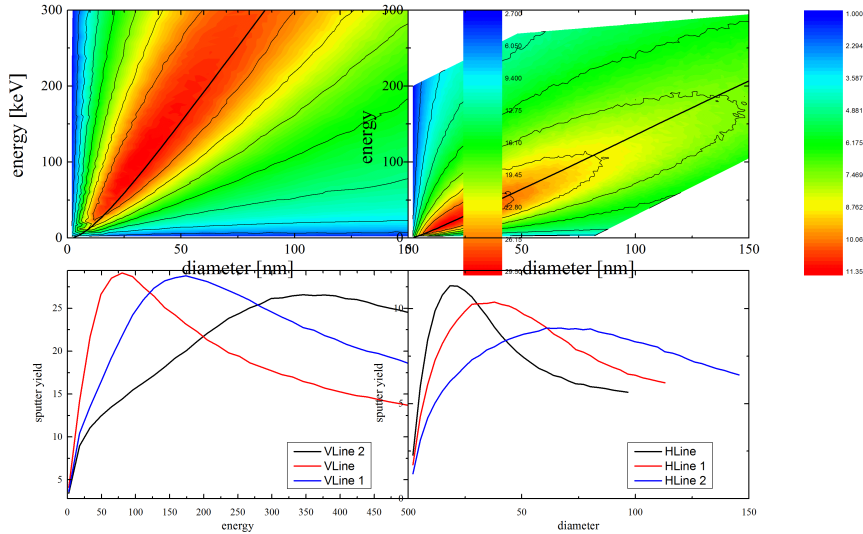


Figure 4.1: a)

where the sputter yield versus energy plot is extracted from the  $Xe^+$  irradiation for a fixed diameter. Here the red, blue and black curves correspond to the irradiation of 25, 50 and 100 nm diameter wires, respectively. The maximum clearly shifts to larger ion energies for larger diameters and is found near the indicated ion range simulated by SRIM. The magenta curve shows the energy dependent sputter yield for a flat *Si* surface irradiated with  $Xe^+$  ions at  $45^\circ$ , and simulated with identical parameters in *iradina*. The global maximum sputter yield is found at  $\approx 100 \text{ keV}$  and  $30 \text{ nm}$ . - *surface maximum*

For Sigmund sputtering model with its Gaussian ellipsoid approximation of the damage profile, a Gaussian peak is fitted to the recoil profile simulated with SRIM for both ions in *Si* [BZH12]. The so found mean damage depth is constantly around 0.7 times the ion range for the whole energy range investigated here. A naive first approximation with the Sigmund sputtering model would predict that the sputtering is maximal where the depth of the damage and the radius of the irradiated nano-

### 4.3 Redeposition

wire coincide. However, this is only true for central impacts, while the simulated situation is an average over all ion-nanowire impact parameters. For non-central impacts there is less of the nanowire ‘in front’ of the ion’s path. Therefore, the maximum of the sputter yield is also at lower energies than it would be for solely central impacts. It is thus a coincidental consequence of the irradiation geometry that ion range is an even better predictor for the diameter of maximum sputtering than the center of the Gaussian fit to the damage distribution. To test the limits of the Sigmund model, a more thorough investigation of the Sigmund model’s predictions for various irradiation scenarios may be interesting, however, since the MD simulations reproduce the reality more realistically anyhow, it will not be undertaken here.

## 4.3 Redeposition

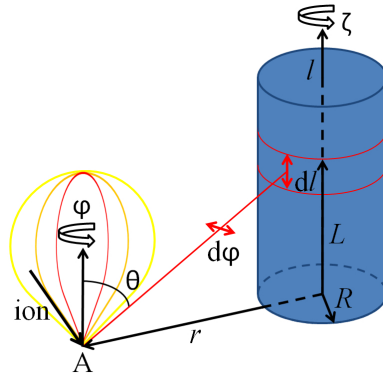
While irradiating a nanowire which is standing perpendicular on a substrate as shown in ?? material will also be sputtered from the substrate. Some of the sputtered material from the substrate will be redeposited on the nanowire, so that the observable sputter yield will be lower than the actual sputtering. Consider the situation shown in figure 4.2. An ion hits the substrate at point A. A possible path of a sputtered atom is indicated by the red line to a point on the nanowire, redepositing the substrate atom on the nanowire.

The following calculation will estimate how many atoms are deposited on the nanowire, by first calculating the probability of a sputtered atom to hit it  $P$ :

$$P = \int_0^{2\pi} \int_0^{\pi/2} H(\theta, \varphi, r, R, L) \tilde{SY}(\theta, \varphi) \cos(\theta) d\theta d\varphi. \quad (4.1)$$

## 4 Sputtering of Nanowires

Figure 4.2: Illustration of the redeposition of sputtered material from the substrate point A onto the nanowire with radius  $R$  at a height  $L$ . Since the wire is rotated around its axis  $\zeta$  and the whole substrate is irradiated, a rotationally symmetric angle distribution for the sputtered atoms can be chosen.



Where  $H(\theta, \varphi, r, R, L)$  is the probability distribution of hitting the nanowire. It is  $1/(4\pi)$  if the trajectory along  $\theta$  and  $\varphi$  from  $r$  hits the nanowire with length  $L$  and radius  $R$ , and zero otherwise. For irradiation at an angle, the angle distribution of the sputter yield  $\tilde{SY}(\theta, \varphi)$  is expected to have a preferential direction along the ion beam [VWMS08]. However, the effective distribution becomes rotationally symmetric (independent of the angle  $\varphi$ ) if one neglects the shadowing of the ion beam on the substrate. Then all points around the wire are hit and the wire is rotated around its axis (angle  $\zeta$ ). This means that a rotationally symmetric angle distribution  $\tilde{SY}(\theta)$  of the sputtered atoms from the substrate can be used, as indicated by the yellow, orange and red bulbs in figure 4.2. A  $\cos^\kappa(\theta)$  distribution is chosen, as it forms flattened angle distributions for  $\kappa < 1$ , which can emulate the rotation of a slanted angle distribution:

$$\tilde{SY}(\theta) = \frac{SY \cdot \cos^\kappa(\theta)}{\int_0^{2\pi} d\varphi \int_0^{\pi/2} \cos^\kappa(\tilde{\theta}) \cos(\tilde{\theta}) d\tilde{\theta}} = SY/c(\kappa) \cdot \cos^\kappa(\theta), \quad (4.2)$$

### 4.3 Redeposition

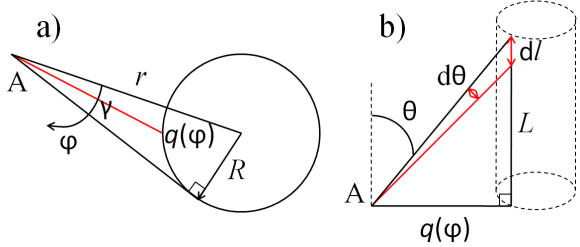


Figure 4.3: a) On the substrate surface  $R$  is the radius of the nanowire,  $r$  the distance from the point of impact  $A$  to the center of the wire,  $q(\phi)$  the distance to the wires surface at the base of the wire. The angle between  $r$  and the tangent to the nanowire circumference is  $\gamma$ . b) Side on view with  $\theta$  the angle to the substrate normal of the trajectory to hit the wire at  $L$ .

where the denominator  $c(\kappa)$  normalizes the angle distribution function  $\cos^\kappa(\theta)$  and  $SY$  is the total sputter yield from the surface. The parametrization of  $H(\theta, \varphi, r, R, L)$  in  $\varphi$  is straightforward, as the integration bounds for  $\varphi$  are  $[-\gamma, \gamma]$  with  $\gamma = \arcsin(R/r)$  the angle between  $r$  and the tangent to the nanowire in figure 4.3a. To solve the integration over  $\theta$  it is useful to express the distance  $q$  from the impact point to the base of the nanowire as a function of  $\rho = R/r$ ,  $r$  and  $\varphi$ :

$$q(\rho, r, \varphi) = r \cdot \sqrt{1 + \rho^2 - 2\sin^2(\varphi) - \sqrt{\cos^2(\varphi)(\cos(2\varphi) - 1 + 2\rho^2)}}. \quad (4.3)$$

Then the integration over  $\theta$  can be substituted by an integration over the length of the nanowire  $l$ . The substitution can be found looking at figure 4.3b:

$$\begin{aligned} d\theta &= \frac{\sin(\theta)}{\sqrt{L^2 + q^2}} dL, \\ \theta &= \arctan(q/L). \end{aligned}$$

#### 4 Sputtering of Nanowires

Inserting into equation 4.1 and simplifying yields:

$$P = \frac{2 SY}{c} \int_0^\gamma \int_{L_1}^{L_2} \frac{l^{\kappa+1} q}{(l^2 + q^2)^{(\kappa+3)/2}} dl d\varphi. \quad (4.4)$$

With  $l^* = L_1 - L_2$  the area hit on the nanowire is now  $\pi R l^*$ , positioned at the height  $L = (L_1 + L_2)/2$  as indicated between the two red lines in figure 4.2. Integrating the probability  $P$  to hit the nanowire at each substrate position over the whole substrate area and normalizing it to the area of the nanowire which is hit yields the number of atoms  $N$  hitting the nanowire per fluence  $\Phi$ :

$$N/\Phi = \frac{2 SY}{c\pi R l^*} \int_0^{2\pi} d\zeta \int_R^\infty \int_0^\gamma \int_{L_1}^{L_2} r \frac{l^{\kappa+1} q}{(l^2 + q^2)^{(\kappa+3)/2}} dl d\varphi dr. \quad (4.5)$$

The integration can be solved numerically using the numerical integration tools CQUAD and QAGI [Gou09]. Perhaps counter-intuitively, the result is independent of the nanowire radius  $R$  and the height at  $L$  at which the deposition is calculated. The redeposition amounts to  $10\% \cdot \Phi \cdot SY$  for the very broad distribution when  $\kappa = 0.25$ . As already shown in figure 4.1c, the sputter yield (SY) is significantly lower on the plane substrate than on the nanowire to begin with. Therefore, the redeposition can be safely neglected for the evaluation of sputtering. As the atoms sputtered from the substrate have a very low energy, they will be deposited on the surface of the nanowire. This makes them prone to re-sputtering, which reduces the finally incorporated number of substrate atoms even further. Nevertheless, care is advised in the choice of the substrate material, as the incorporation of substrate atoms in the nanowire may have detrimental doping effects.

#### 4.4 *Si* nanowire sputtering by $Ar^+$ irradiation

## 4.4 *Si* nanowire sputtering by $Ar^+$ irradiation

The experimental verification of the diameter dependent maximum in sputtering was investigated on etched *Si*-nanowire arrays. Figure 4.4a shows the principle irradiation setup illustrated by a SEM image of a single nanowire before and after the irradiation with  $300\text{ keV }Ar^+$ . The etched nanowire samples and the RHT allowed the simultaneous, rotated irradiation of upstanding nanowires with various diameters at  $300^\circ C$ . Figure 4.4b shows the extracted and aligned diameter versus height profile for the nanowire in figure 4.4a. More than 100 such profiles were semi-automatically extracted for many different nanowire diameters. The sputter yield calculated from these extracted profiles is plotted versus the local diameter in 4.4c for 100 and  $300\text{ keV }Ar^+$ .

The experimental sputter yield reproduces the qualitative, simulated diameter dependence of the sputter yield well. The maximum sputtering is found for those nanowire diameters where the diameter corresponds to the ion range, just as discussed in chapter 4.2 and the Sigmund sputtering model in chapter 2.1. The interruptions and discontinuities for diameters  $< 50\text{ nm}$ , at  $\approx 200\text{ nm}$ ,  $\approx 300\text{ nm}$  and  $\approx 500\text{ nm}$  are located where the diameter range of an array of nanowires on the irradiated substrate ended. Here, there are fewer (none for 100 keV and  $\approx 200 - 300\text{ nm}$ ) nanowires which could be evaluated.

The large variance indicated in figure 4.4c as ‘error-bars’ can be attributed to the fact that the observed diameter changes of around  $5\text{ nm}$  are close to the resolution limit of the SEM at  $2\text{ nm}$ . Therefore, the observation of a sensible sputter yield value is only possible with the large number,  $> 1000$ , of diameters evaluated. Nevertheless, sputter yields around 0, as found in the experimental values at  $400\text{ nm}$  are not realistic. They have to be attributed to misalignment and remaining focal plane, brightness and contrast differences between the SEM im-

#### 4 Sputtering of Nanowires

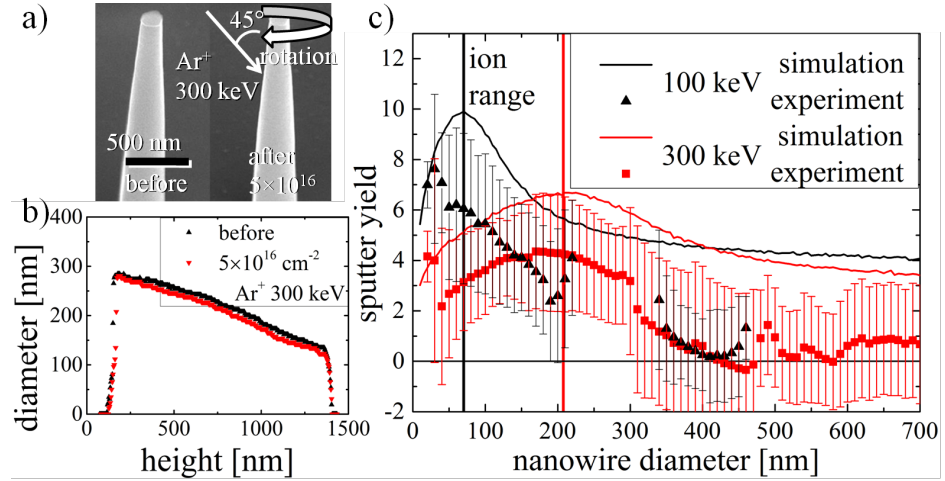


Figure 4.4: a) Exemplary SEM images of a *Si* nanowire before and after the rotated irradiation with 300 keV  $\text{Ar}^+$  at 300°C. The extracted diameter vs. height profile for this nanowire is shown in b). From many such profiles the sputter yield vs. diameter was calculated and plotted in c) as black triangles and red squares for the irradiation with 100 and 300 keV  $\text{Ar}^+$ , respectively. The ‘error bars’ indicate the variance of the data points grouped together every 10 nm. The sputter yield calculated with *iradina* simulations is shown for either case as a line-plot. The corresponding SRIM ion range at 45° is marked by a vertical line.

ages before and after irradiation which could not be corrected in the image analysis. Because of these systematic deviations, the variance is a more useful estimation at the accuracy of the experimentally determined sputter yield than the more usual standard deviation which would underestimate the experimental error considerably.

The quantitative discrepancy between the simulated sputter yield and the experimental values is not unexpected. To start with, the quantitative value from the *iradina* simulation was discussed in chapter 2.2 to be questionable. Nevertheless, the main contribution to a systematic deviation in the experimentally evaluated sputter yields is the oxidation of the *Si* nanowires in air between the subsequent irradiation and SEM

#### *4.5 Discussion*

investigation steps. The thickness of oxidized *Si* on the surface of the nanowires is significant but dependent on uncontrolled factors such as humidity and temperature [Luk72, ABORvdBA91]. As all the oxygen in the oxidized layer of the nanowires also has to be sputtered away, the experimental procedure will underestimate the sputter yield.

Finally, the fact that the experimentally observed sputter yield has its maximum at slightly lower diameters than the simulated values for both the 100 *keV* and 300 *keV* irradiations may indicate the occurrence of cluster and thermal sputtering. Both have been predicted with MD simulations [NSUM14, UBNM15, ABU15], albeit in nanostructures with much smaller dimensions. As the kinetic energy of the ion is, on average, distributed to less material in nanowires with smaller diameters, both cluster and thermal sputtering are larger for smaller nanowire diameters.

## **4.5 Discussion**

# **5 High Doping Concentrations in Nanowires**

## **5.1 Doping and Sputtering**

## **5.2 Pseudo-dynamic simulation**

## **5.3 Results from optimal irradiation conditions**

## **5.4 Discussion of relevant effects**

redeposition from substrate (numeric Simulation)  
shadowing with old results

### **Discussion**

# 6 Plastic Flow in Silicon Nanowires

## 6.1 Discovery

Within the “wiring quantum dots” project *Si* nanowires were irradiated with  $As^+$  and  $In^+$  and/or  $Ga^+$  so that in a subsequent annealing step  $Si - GaAs$  or  $Si - InGaAs$  hetero-structures could be formed. Markus Glaser, the Ph.D. student responsible for this part of the project, had developed a good habit of making SEM images of the same individual wires after each process step. We thus noticed, that the *Si* nanowires shrank quite dramatically during the irradiation with  $\approx 100\text{ keV}$   $In^+$ ,  $Ga^+$  and  $As^+$  at room temperature. Two examples of this can be seen in figure 6.1. A look into literature revealed that this behavior has so far not been reported for irradiation of *Si* at such low ion energies. A thorough investigation might be worthwhile.

Similar *Si* nanowire arrays as the ones used for the sputtering experiment were thus systematically irradiated with  $Ar^+$ , making SEM images after each irradiated fluence to observe and quantify the deformation.  $Ar$  was chosen for the irradiation to avoid any chemical effects and because it has a comparable mass to *Ga* and *As*. Using the algorithm described in the sputter yield chapter, the profiles for the irradiated nanowires could be extracted. In figure 6.2 the black, red, green and blue lines

## 6 Plastic Flow in Silicon Nanowires

Figure 6.1: placeholdergraph - get nicer image from Markus. SEM images of VLS-grown *Si*-nanowires before and after the irradiation with X In and Y As at room temperature, while rotating the sample. The shrinking and widening of the wires is clearly visible. In the background wires which were not aligned perpendicular to the substrate are bent upward.

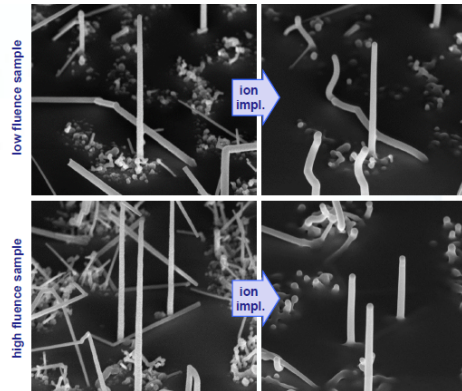
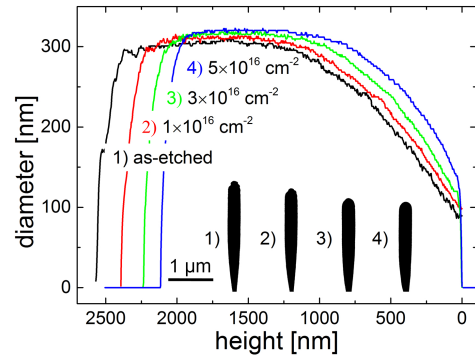


Figure 6.2: Graphs of the diameter over height of a single *Si* nanowire irradiated with increasing fluences of  $100\text{ keV Ar}^+$  ions. The black insets show the profiles of the nanowire after the respective fluences extracted from SEM images. In both illustrations the shrinking and widening of the wire is clearly visible.



indicate the height dependent diameter of a single wire before and after irradiation with  $100\text{ keV Ar}^+$  up to fluences of 1, 3 and  $5 \times 10^{16}\text{ cm}^{-2}$  respectively. In this graph, as well as in the inset black profiles, the reduction of the height by  $\approx 500\text{ nm}$  and an increase of the diameter, especially at the base, can be clearly seen. The deformation is only seen with irradiation at room-temperature where *Si* amorphization threshold of  $10^{14}\text{ ions/cm}^2$  for  $100\text{ keV Ar}^+$  is very low [PMB04].

## 6.2 Quantification of the Deformation

The deformation of the nanowires can be roughly quantified by fitting a linear trend to the fluence dependence of the height of the wires. This

## 6.2 Quantification of the Deformation

yields an average of 3% shrinkage per  $10^{16} \text{ ions}/\text{cm}^2$ . Due to outliers with larger deformation the values obtained for the 21 nanowires investigated have a large standard deviation of  $\pm 3\%$  shrinking per  $10^{16} \text{ ions}/\text{cm}^2$ . A more thorough investigation of the deformation is possible by also accounting for the height dependence of the diameter seen in figure 6.2. On average a certain number of atoms are displaced by a certain distance along the height  $z$  of the nanowire per ion. Considering only the movement along the height  $z$ , a mass-transport rate (MTR) can be calculated according to equation 6.1:

$$\begin{aligned} MTR_{(1 \rightarrow 2)} &= [{}^1N \cdot {}^1z_c - {}^2N \cdot {}^2z_c - ({}^1N - {}^2N) \cdot {}^2z_c]/N_{ion} \\ &= {}^1N \cdot ({}^1z_c - {}^2z_c)/N_{ion} \end{aligned} \quad (6.1)$$

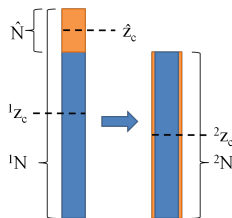


Figure 6.3: Illustration of the mass-transport rate calculation. Displacing  ${}^1N$  atoms from their average height  ${}^1z_c$  to the average height  ${}^2z_c$  requires the same mass-transport, as moving  $\hat{N}$  from  $\hat{z}_c$  to  ${}^2z_c$ , taking into account the sputtered atoms  ${}^1N - {}^2N$ .

In equation 6.1 and figure 6.3,  ${}^{1/2}z_c$  is the height of the center of mass of the nanowire with the top left index indicating before ( $^1$ ) and after ( $^2$ ) irradiation respectively. The number of atoms at height  $z_i$  can be calculated from the local radius  $r_i$ . Summing up the height weighted by the number of atoms at that height  $z_c \cdot N = \sum_i \pi r_i^2 h \cdot \rho \cdot z_i$  and dividing this by the total number of atoms  $N = \sum_i \pi r_i^2 h \cdot \rho$  in the nanowire gives us  $z_c$ . The sums are over all slices  $i$  of height  $h = 1 \text{ pixel} = 2.7 \text{ nm}$  (typically) each. The number of ions that hit the nanowire in the irradiation of fluence  $\Phi_{12}$  between making SEM images 1 and 2 is  $N_{ion} = \sum_i ({}^1r_i + {}^2r_i) \cdot \sin(45^\circ) \cdot h \cdot \Phi_{12}$ . The last term in equation 6.1 accounts for the influence of sputtered atoms. Just as in the chapter

## 6 Plastic Flow in Silicon Nanowires

on sputtering, the sputter yield could be calculated by  $(^1N - ^2N)/N_{ion}$ . Figure 6.3 illustrates two interpretations of the MTR calculation. As only the displacement along  $z$  is considered, the direct interpretation of equation 6.1 of moving  $^1N$  atoms from their center of gravity  $^1z_c$  to a new center of gravity  $^2z_c$  is equivalent to moving the atoms which are ‘missing’ at the top of the wire after the irradiation ( $\hat{N}$ , orange volume in figure 6.3) from their center of gravity  $\hat{z}$  to  $^2z_c$ , and subtracting the sputtered atoms. This evaluation yields an average mass-transport rate of  $1.2 \cdot 10^4 \text{ atoms} \cdot \text{nm}/\text{ion}$  with a standard deviation of  $7 \cdot 10^3 \text{ atoms} \cdot \text{nm}/\text{ion}$ . Again the large standard deviation is due to outliers with larger deformation.

### 6.3 Knock-on transport of mass

A possible explanation for this behavior can be sought in the linear cascade theory which is applicable for the cascades of  $100 \text{ keV } Ar^+$  in *Si*. In a collision cascade following an energetic ion impinging a solid, atoms will be preferentially ‘knocked-on’ along the propagation direction of the impinging ion. This causes an inhomogeneous distribution of interstitials and vacancies and effectively mass is transported ‘downstream’ along the ion beam. In an amorphous material it is not clear what constitutes an ‘interstitial’ or a ‘vacancy’, but a local excess of vacancies can be understood as a locally decreased density, while an interstitial excess corresponds to an increased density. A local density gradient is not stable, since the density of amorphous *Si* before and after irradiation is not significantly different [PMB04]. Therefore, the density gradient introduces stress in the material which can relax by plastic deformation, possibly enabled by a decreased viscosity due to further ion irradiation [SBB97, HCA02, MAAA03, MA03].

### 6.3 Knock-on transport of mass

As was shown in the example of sputtering, BCA simulation software can accurately reproduce linear collision cascades. Therefore, comparing the experiments with a simulation with *iradina* can evaluate whether the deformation observed in the experiment can be accounted for by knock-on mass transport. Figure 6.4a shows the simulation volume implemented in *iradina* with  $2 \times 2 \times 2 \text{ nm}^3$  voxels as a  $600 \text{ nm}$  long *Si* cylinder with a diameter of  $200 \text{ nm}$ . The  $100 \text{ keV Ar}^+$  ions impinge at an angle of  $45^\circ$  to the  $z$ -axis. They strike the cylinder distributed uniformly along the  $y$ -direction at height  $z = 0$ . Figure 6.4d shows the resulting distribution of interstitials on the cross-sectional slice through the middle of the nanowire along the  $xz$  plane. This can be seen as an approximation for the distribution of the nuclear energy loss and shows the mean extent of the collision cascade. Figure 6.4e shows the same cross-section after subtracting the number of vacancies produced per ion from the number of interstitials. The excess of vacancies along the impinging plane (blue cone in the cross section) enveloped by two red planes of excess interstitials shows that there is a high probability for the ions to hit a target atom with a large impact parameter. This changes the ions path only little and displaces the target atom in a direction perpendicular to the ion beam. Superimposing many collisions along the  $y$  direction leads to the formation of one one vacancy rich and two interstitial rich planes. The  $xy$ -plane in 6.4b shows the sum over the height  $z$  of the difference between interstitials and vacancies plotted to the same color scale. The illustration is dominated by vacancies at the surface of the cylinder which are left behind by sputtered atoms.

The height distribution (summing over the radial  $xy$  plane) of the interstitials, vacancies and leaving atoms is shown in 6.4c. As expected, the majority of sputtered atoms originate near the impact height. The lines showing the interstitials and vacancies overlap in this illustration. The vacancies subtracted from the sum of interstitials and leaving atoms

## 6 Plastic Flow in Silicon Nanowires

is plotted along the height in 6.4f. As a displaced atom, leaving behind a vacancy, is either sputtered or becomes an interstitial, the sum over all heights of of this graph is zero. The strong oscillation around  $z = 0$  in 6.4f is caused by the previously discussed displacement of target atoms at an angle almost perpendicular to the ion beam for large impact parameters. This oscillation is very sensitive to the voxel-size as in effect the voxel size defines a recombination length and interstitial and vacancy rich regions are mixed in larger voxels. On the other hand, the excess of vacancies near the impact point ( $\leq 70\text{ nm}$ ) and of interstitials further down along the ion's path ( $\approx 100\text{ nm}$ ) is not sensitive to the voxel size. It can be used to quantify the knock-on mass transport by multiplying the plotted values by their height and integrating over all heights. The influence of the short range oscillation immediately around the impact point disappears as here  $z \approx 0$  is small. The value obtained from this calculation is  $78 \pm 1 \text{ atoms} \cdot \text{nm/ion}$ . Clearly this value is to low to account for the large deformation observed in the experiment where a mass-transport rate of  $\geq 1 \times 10^4 \text{ atoms} \cdot \text{nm/ion}$  was assessed.

#### *6.4 Irradiation at large angles of incidence*

For all simulations a reasonable value for crystalline *Si*, 15 eV [CW65], was used for the displacement energy which governs the creation of interstitials and vacancies in the simulation, as discussed in chapter 2.2. However, in amorphous materials it is questionable what this value is supposed to mean, as point defects are not well defined. Therefore, simulations were repeated with the displacement energy set to 0 eV. As expected, the number of ‘vacancies’ and ‘interstitials’ now produced by the simulation increased dramatically. However, the long range difference between ‘vacancies’ and ‘interstitials’ seen in figure 6.4f is unchanged. This is an indication that the knock-on mass transport is dominated by the rare events where target atoms are hit directly by the impinging ions. In these cases, a large amount of energy is transferred to the displaced atom leading to a long trajectory within the material. The atoms displaced with lower energies are much more numerous, but travel much shorter distances and in a randomly orientated direction. This is because most of the low energy displaced atoms are generated at the end of a branch of the collision cascade, the orientation of the branch having previously been randomized by higher energy collisions. And/or they originate from collisions with a high impact factor, which lead to a large angle between the incoming particle’s and the displaced particle’s momentum, as seen in the separation of interstitials and vacancies near the impact point in figure 6.4e.

## **6.4 Irradiation at large angles of incidence**

If knock-on mass-transport is not the main contribution to the deformation, the question arises whether the direction of the deformation is related to the ion beam. Will an irradiation from ‘below the substrate’ towards an unconstrained end of the nanowire would also shrink the wire,

## 6 Plastic Flow in Silicon Nanowires

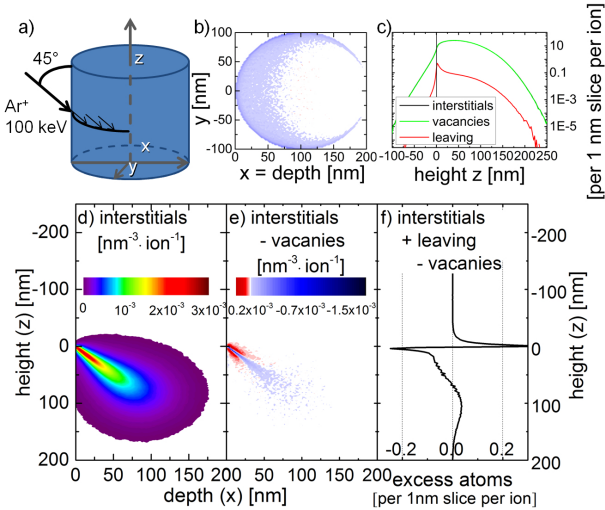


Figure 6.4: a) Illustration of the simulated irradiation geometry. All  $Ar^+$  ions of  $100\text{ keV}$  energy hit the nanowire volume at the same height and at an angle of  $45^\circ$  with respect to the wire axis  $z$ . The created interstitials in the radial cross-section through the middle of the simulated nanowire is shown in d). This distribution is effectively an illustration of the nuclear energy loss. In e) the vacancies are subtracted from the interstitials for the same cross-section. Summing this difference over all heights gives the radial distribution shown in b). The clear dominance of vacancies near the surface is caused by sputtering. The axial profile of the interstitials, vacancies and leaving (sputtered) atoms plotted in c) over the height relative to the impact plane shows that most atoms are sputtered at the impact height. Note that the plots of vacancies and interstitials overlap. The vacancies subtracted from the sum of interstitials and sputtered atoms plotted over the height in f) shows mass transport along the ion's path. Apart from the strong oscillation at the impact height, there is a deficiency of atoms close to the impact height ( $\leq 70\text{ nm}$ ) and an excess centered around  $100\text{ nm}$  down from the impact height.

## 6.4 Irradiation at large angles of incidence

or stretch it out? Nanowires attached to a substrate are obviously not suited to testing this, so a method to irradiate nanowires while rotating them at angles greater than  $90^\circ$  to the ion beam was devised. This was achieved by attaching a *Si* nanowire grown epitaxially on a *Si* wafer to an *Au* microwire which can suspend the nanowire at arbitrary angles in the irradiation chamber. The process is shown in figure 6.5. The *Pt* deposition was used to glue the nanowire to the micro-manipulator in the FIB and cut the nanowire from the substrate with the *Ga*-FIB. Using the *Pt*-deposition and *Ga*-FIB again, the nanowire is subsequently attached to the tip of a sharpened *Au*-microwire which was previously glued to a piece of wafer for handling and also placed in the FIB chamber. VLS-grown nanowires were used for this experiment as they were readily available in longer lengths ( $> 10\mu m$ ) than the etched nanowires.

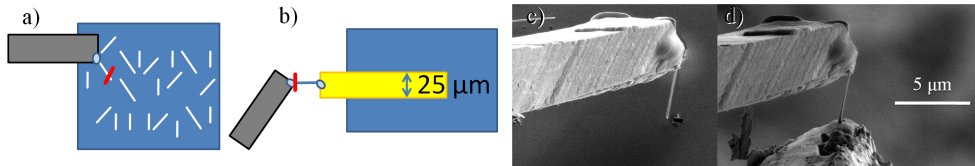


Figure 6.5: Illustration of the nanowire-on-microwire fabrication in a FIB system. The schematic a) and SEM image c) show the wire first glued to the micro-manipulator in the FIB by *Pt*-deposition (light blue ellipse), then cut from the substrate with the *Ga*-FIB (red line). Images b) and d) illustrate the subsequent gluing to an *Au* microwire with *Pt*-deposition and the final cut with the *Ga*-FIB to release the nanowire from the micro-manipulator.

The nanowire-on-microwire samples consisted of typically  $3 - 5$  nanowires, each attached to an *Au*-microwire and arranged in the irradiation chamber on a rotatable stage at an angle of  $135^\circ$  to the ion beam, as shown in figure 6.6a. The alignment of the nanowires to their microwire support was found to be crucial, as any shadowing of a nanowire from the ion beam on one side would lead to extreme bending of the wire. Only a single wire was found straight enough to evaluate quantitatively

## 6 Plastic Flow in Silicon Nanowires

for more than one irradiation step. The SEM images of this wire are shown in figure 6.6b-f view from a perspective perpendicular to the axis of rotation and rotated by the indicated angle around this axis. The left SEM images show the unirradiated nanowire, while the center and right images were made after the irradiation of  $1 \times 10^{16} \text{ cm}^{-2}$  and  $3 \times 10^{16} \text{ cm}^{-2}$   $100 \text{ keV Ar}^+$ , respectively. The unirradiated wire is straight and  $3.9 \mu\text{m}$  long. The irradiated wire shows some bending, so the length had to be determined from a perspective where the curvature of the wire is in plane with the image. A fifth order polynomial was fitted to the bent shape and the length of the wire was thus determined to be  $3.5 \mu\text{m}$  after  $1 \times 10^{16} \text{ cm}^{-2}$  (6.6b) and  $3.2 \mu\text{m}$  after  $3 \times 10^{16} \text{ cm}^{-2}$  (6.6f). The nanowire thus shrank with a similar deformation rate to the previously reported 3% strain per  $10^{16} \text{ ions/cm}^2$ , even though the irradiation was directed towards its free end.

This experiment shows with certainty that the knock-on mass-transport is not the main contributor to the observed deformation, as it would have to be directed along the ion beam. The discussion of a possible model for the deformation will be easier by addressing similar effects and the way that simulation tools were used to understand them. The BCA MC simulation tools available inherently neglect all collective movement of atoms within the target. As has been shown in the previous two chapters, this may be sufficient for the prediction of sputtering and the ion distribution in nanostructures. A field of study which has already faced the limitation of neglecting the local temperature in ion irradiation is the irradiation with swift, heavy ions. At energies well beyond  $\text{MeV}$  the assumption that the dominating effects will be described by binary collisions between the ion and target atoms is false. At these high energies and ion masses a significant amount of energy will be transferred from the ion to the electronic system of the target. Through the relaxation mechanisms of the electronic system a part of this energy will be

#### 6.4 Irradiation at large angles of incidence

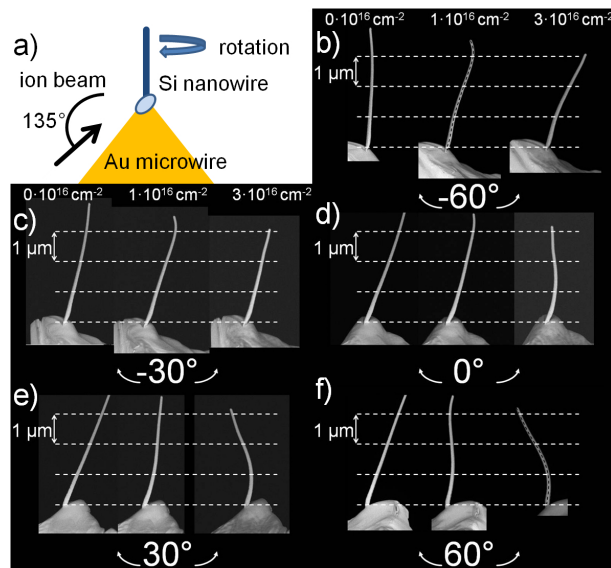


Figure 6.6: a) Illustration of the nanowire-on-microwire irradiation setup. b) - f) SEM images of the same nanowire as-mounted (left SEM images), after irradiation with  $1 \times 10^{16} \text{ cm}^{-2}$  (center images), and  $3 \times 10^{16} \text{ cm}^{-2}$  (right images)  $100 \text{ keV Ar}^+$  ions. The SEM images were taken with the nanowire rotated by the indicated angle from a perspective perpendicular to the angle of rotation. The length of the nanowire after irradiation is determined in b) and f) along the dashed lines.

## 6 Plastic Flow in Silicon Nanowires

converted to heat in the lattice. Under certain conditions this will form “ion-tracks” in the target. One approach to understanding the formation and behavior of ion-tracks is to simulate the longitudinal distribution of the deposited ion energy in the target with BCA tools (typically SRIM) and to evaluate the local temperature in a second step by following the deposited energy according to thermodynamic considerations. A good review of such “thermal spikes” can be found in [WKW04].

Such a thermal spike approach was successful at understanding the plastic deformation by swift heavy ion irradiation according to Trinkaus and Ryazanov [TR95] and in the understanding of material properties governing the direction of the deformation [HKW04, HKW05]. When nanoparticles are deformed [SvBvD<sup>+</sup>00, SvBvD<sup>+</sup>01, vDSF<sup>+</sup>01, DPFB01, DPKB03, DDP<sup>+</sup>04] an adapted version of the model by Trinkaus can be applied and the effect dubbed “ion hammering” [Kla04]. In short, according to this model the local temperature leads to a transient ‘liquid’ phase in the cylindrical volume of material around the ion’s path. Within the cylindrical geometry, the deformation by thermal expansion is anisotropic and because stresses can relax in the low viscosity volume, this is a plastic deformation. This is not observed in materials which remain crystalline during the irradiation, as the long range order of the crystal lattice is reinforced upon the recrystallization during cooling. The problem with directly applying this model to the situation at hand is that the total energy density in the collision cascade of 100 keV Ar<sup>+</sup> in *Si* is a low  $\frac{dE}{dx} = 36 \frac{eV}{nm}$ , of which the electronic energy loss is roughly half. Also, the lowest ion energy for which plastic deformation of silica nanoparticles is reported is 300 keV Xe<sup>+</sup> [DPKB03]. Here the energy loss is merely  $\frac{dE}{dx} = 120 \frac{eV}{nm}$  with 20 % lost to the electronic system. The threshold for ion tracks, however, is given at  $\frac{dE}{dx} \geq 1 \frac{keV}{nm}$  by Trinkaus et al. [TR95]!

#### 6.4 Irradiation at large angles of incidence

The alternative to thermodynamic considerations after a MC BCA simulation are full MD simulations, where the trajectory and interaction of every atom or ion in the simulation volume is followed. This naturally includes all thermal effects, but is limited by computing power to a low number of atoms and thus a severely limited volume of material. Additionally the accuracy of results depends greatly on finding the interaction potential for all combinations of ions and atoms involved. Here again, as for sputtering, this is true especially for low energy interactions, where these potentials are not available but a topic of research in themselves [Pri12, PGB13]. Investigations of the self-irradiation of  $10\text{ keV Si}$  and various metals [NGA<sup>+</sup>98] revealed the formation of nanoscale ‘liquid’ pockets. The term “liquid” must be used with care as it refers to a thermodynamical state of matter while the simulation timescale does not allow the assumption of thermodynamic equilibrium. Nevertheless, a sufficiently large number of atoms gain much kinetic energy (say ‘are hot’) to make the assumption of reduced viscosity and other effects safe. The interesting point of this example is that the energy in the collision cascade was quite low, so that the trajectory of the initiating particle could also have been accurately simulated according to the BCA. A more recent MD investigation by Baumer et al. gets even a step closer to the presented experimental results, in that it predicts plastic deformation in metallic glasses irradiated with high energy neutrons [BD14]. The collision cascades are initiated in  $a\text{-Cu}_{50}\text{Nb}_{50}$  by assuming primary knock-on atoms of  $475\text{ keV Nb}$ . This atomistic study explicitly shows that plastic deformation due to thermal expansion and stress relaxation can be anisotropic also in collision cascades which do not have the high energy density and symmetry required by the Trinkaus model [TR95]. Some-what contrary results were obtained by Mayr et al. [MAAA03] where  $10\text{ eV}$  to  $100\text{ keV}$  recoils of  $\text{Cu}$  and  $\text{Ti}$  in  $a\text{-CuTi}$  were simulated. That study comes to the conclusion that the viscous flow is dominated by

## 6 Plastic Flow in Silicon Nanowires

ion induced point defects. It does not propose that knock-on atoms are initiate the deformation, but rather, that thermal effects do not provide the main contribution to the reduced viscosity observed during ion irradiation.

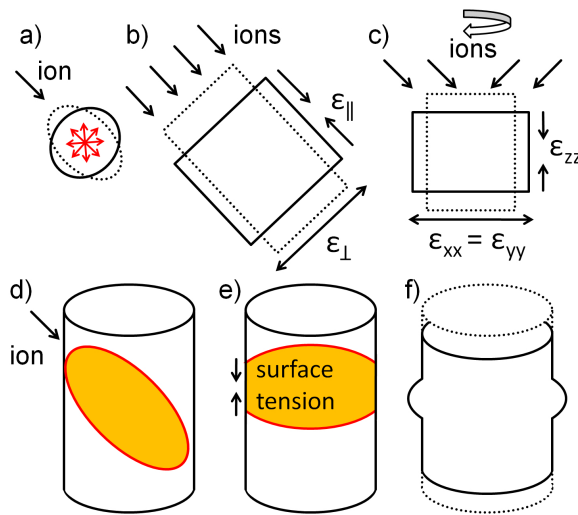


Figure 6.7: a) - c) Illustration of a deformation model analogous to ion hammering. a) The collision cascade from a single impinging ion heats an approximately ellipsoidal volume of the target material. The internal pressure will lead to an expansion towards a more spherical shape which is retained upon cooling. b) The net effect of many ions is thus a contraction parallel to and an expansion perpendicular to the ion beam. For no change in density  $\epsilon_{\parallel} = -2\epsilon_{\perp}$  has to hold. c) Under rotational symmetry this deformation translates to a contraction in the rotational axis  $z$  and an expansion in the perpendicular  $x - y$  plane with  $\epsilon_{zz} = -2\epsilon_{xx} = -\epsilon_{\perp}$ . In d) - f) the alternative, surface tension driven deformation is illustrated. The collision-heated volume of target material shown in d). A significant slice of the wire shown in e) thus has a reduced viscosity. The surface energy is reduced by an increase in the local diameter of the wire, leading to a shortened and thickened wire segment shown in f).

## 6.5 The deformation mechanism

The effect of anisotropic deformation within the collision cascade induced by the irradiation of nanowires is shown in figure 6.7a - c. An approximately ellipsoidal volume of the target material is heated by the collision cascade. It expands, becoming more spherical and the anisotropic deformation is retained after cooling. The superimposition of many collision cascades with a similar effect leads to a net contraction along the ion beam  $\epsilon_{\parallel} < 0$  and an expansion perpendicular to it  $\epsilon_{\perp} > 0$  as shown in 6.7b. To maintain constant density  $-2 \cdot \epsilon_{\perp} = \epsilon_{\parallel}$ . The rotational average of this deformation around the  $z$ -axis, as illustrated in 6.7c, works out to be a contraction along the  $z$ -axis  $\epsilon_{zz} = \frac{1}{2}\epsilon_{\parallel}$  and a corresponding expansion in the  $xy$ -plane for an angle of  $\pm 45^\circ$  between the ion beam and the  $z$ -axis. The  $z$ -axis represents the nanowire axis, while the  $xy$ -plane is parallel to the nanowire diameter. Thus the deformation rate of  $\frac{d\epsilon_{zz}}{d\Phi} = 3\%$  strain per  $10^{16} \text{ ions/cm}^2$  extracted from a linear fit to the reduction of the nanowire height can be transformed into a strain rate parallel to the ion beam of  $\frac{d\epsilon_{\parallel}}{d\Phi} = 6\%$  strain per  $10^{16} \text{ ions/cm}^2$ . This is much less than the values reported for the studies at higher energies reported in literature. In ref. [DPKB03]  $10^{-16} \text{ cm}^2/\text{ion}$  were reported for  $300 \text{ keV Xe}$  in silica nanoparticles and ref. [BD14] even arrives at  $10^{-15} \text{ cm}^2/\text{ion}$  with MD calculations in bulk. There are unfortunately no studies published on straining bulk silicon at these low ion energies. The bending of thinned  $Si$ -wafers similar to [Vol91, MKKP08] would be measurable with the a straining rate of 6% strain per  $10^{16} \text{ ions/cm}^2$  in a layer of  $\approx 300 \text{ nm}$ .

The quantitative discrepancy between the deformation observed in the experiments presented here and published studies may be attributed to the lower ion energy and one may gain confidence in this model due to the qualitative similarity to the MD simulations by Baumer et

## 6 Plastic Flow in Silicon Nanowires

al. [BD14] also showing deformation anisotropy at relatively low ion energies. However, a further, major concern is the fact that in the presented experiments the collision cascade is not in bulk, but in a nanostructure where there is not much material around and it is not distributed around the cascade isotropically. If the ellipsoidal volume intersects the nanowire surface, the pressure from the thermal expansion will vent outward removing the force needed to drive the deformation. A more favorable model illustrates that the strong influence of the surface expected in nanowires can also lead to the observed plastic deformation. In figure 6.7d the relation between the nanowire and collision cascade is shown. As there is not much material around, the temperature in a sizable slice of the nanowire will remain elevated for some time [Bor12, GHB<sup>+</sup>13, ABU15, JHMR15]. In addition the ion irradiation will further reduce the viscosity [SBB97, HCA02, MAAA03], allowing the surface tension to deform the nanowire by increasing the radius locally. The local increase in diameter reduces the total surface area and thus the surface energy. The wire subsequently becomes shorter and wider as shown in figure 6.7f.

Apart from the bulk deformation experiment already suggested, a further experiment which could distinguish which of the two models applies is the irradiation of the nanowires at 90° between the nanowire axis and the ion beam. In this case if the first model similar to ion hammering applies the irradiation should produce slowly elongating wires with a reduced radius, as the positive  $\epsilon_{\perp}$  is now parallel to the nanowire axis. On the other hand, if the surface tension driven model is applicable the nanowires will shrink regardless of the irradiation angle. Naturally, a similar nanowire-on-microwire setup to the one for irradiation at 135° could be used to irradiate at 90°. It turns out however, that the irradiation at 90° is extremely prone to bending the nanowires. Due to the bending, the angle between the nanowire and the ion beam varied

## *6.5 The deformation mechanism*

during a rotation cycle so that a conclusive discrimination between the models can unfortunately not be made. The bending can be attributed to the *Pt* deposited to glue the *Si* nanowire onto the *Au* microwire in the FIB. This deposition is concentrated at the base and on one side of the nanowire and thus suppresses the rotational symmetry of the deformation, leading to bending. In the irradiation at 135° the base of the wire, where it is glued to the microwire, is shadowed from the ion beam by the microwire so that the nanowires are less likely to bend.

## **Discussion**

## 7 Summary and Outlook

*check: Master Thesis Noack, Ogrisek, Conference proceeding D. Sage, Rutherford, Nordlund*

# Bibliography

- [ABORvdBA91] Amir H. Al-Bayati, Kevin G. Orrman-Rossiter, J.A. van den Berg, and D.G. Armour. Composition and structure of the native Si oxide by high depth resolution medium energy ion scattering. *Surface Science*, 241(1-2):91–102, January 1991.
- [ABU15] Christian Anders, Eduardo M. Bringa, and Herbert M. Urbassek. Sputtering of a metal nanofoam by Au ions. *Nuclear Instruments and Methods in Physics Research Section B: Beam Interactions with Materials and Atoms*, 342:234–239, January 2015. 00000.
- [ANNK02] Karsten Albe, Kai Nordlund, Janne Nord, and Antti Kuronen. Modeling of compound semiconductors: Analytical bond-order potential for Ga, As, and GaAs. *Physical Review B*, 66(3):035205, July 2002.
- [AW59] B. J. Alder and T. E. Wainwright. Studies in Molecular Dynamics. I. General Method. *The Journal of Chemical Physics*, 31(2):459–466, August 1959. 01183.
- [BD14] Richard E. Baumer and Michael J. Demkowicz. Prediction of Spontaneous Plastic Deformation of Irradiated Metallic Glasses due to Thermal Spike-Induced Plastic-

## Bibliography

- ity. *Materials Research Letters*, 2(4):221–226, October 2014.
- [BDSS04] M. Borgström, K. Deppert, L. Samuelson, and W. Seifert. Size- and shape-controlled GaAs nano-whiskers grown by MOVPE: a growth study. *Journal of Crystal Growth*, 260(1–2):18–22, January 2004.
- [BH88] R. Mark Bradley and James M. E. Harper. Theory of ripple topography induced by ion bombardment. *Journal of Vacuum Science & Technology A*, 6(4):2390–2395, July 1988.
- [BHK<sup>+</sup>10] Thomas M. Babinec, Birgit J. M. Hausmann, Mughees Khan, Yinan Zhang, Jeronimo R. Maze, Philip R. Hemmer, and Marko Lončar. A diamond nanowire single-photon source. *Nature Nanotechnology*, 5(3):195–199, March 2010.
- [Bie87] J. P. Biersack. Computer simulations of sputtering. *Nuclear Instruments and Methods in Physics Research Section B: Beam Interactions with Materials and Atoms*, 27(1):21–36, June 1987.
- [BMB<sup>+</sup>11] Christian Borschel, Maria E. Messing, Magnus T. Borgstrom, Waldomiro Paschoal, Jesper Wallentin, Sandeep Kumar, Kilian Mergenthaler, Knut Deppert, Carlo M. Canali, Hakan Pettersson, Lars Samuelson, and Carsten Ronning. A New Route toward Semiconductor Nanospintronics: Highly Mn-Doped GaAs Nanowires Realized by Ion-Implantation under Dynamic Annealing Conditions.

## Bibliography

- Nano Letters*, 11(9):3935–3940, September 2011.  
WOS:000294790200073.
- [BMS<sup>+</sup>06] C. Borchers, S. Müller, D. Stichtenoth, D. Schwen, and C. Ronning. Catalyst Nanostructure Interaction in the Growth of 1d ZnO Nanostructures. *The Journal of Physical Chemistry B*, 110(4):1656–1660, February 2006.
- [BMS<sup>+</sup>08] Ivan Bizyukov, Andreas Mutzke, Ralf Schneider, Alexander M. Gigler, and Karl Krieger. Morphology and changes of elemental surface composition of tungsten bombarded with carbon ions. *Nuclear Instruments and Methods in Physics Research Section B: Beam Interactions with Materials and Atoms*, 266(9):1979–1986, May 2008. 00007.
- [Bor12] Christian Borschel. *Ion-Solid Interaction in Semiconductor Nanowires*. PhD thesis, University Jena, Jena, 2012.
- [BR11] C. Borschel and C. Ronning. Ion beam irradiation of nanostructures – A 3d Monte Carlo simulation code. *Nuclear Instruments and Methods in Physics Research Section B: Beam Interactions with Materials and Atoms*, 269(19):2133–2138, October 2011.
- [BSL<sup>+</sup>11] Christian Borschel, Susann Spindler, Damiana Lerose, Arne Bochmann, Silke H. Christiansen, Sandor Nietzsche, Michael Oertel, and Carsten Ronning. Permanent bending and alignment of ZnO nano-

## Bibliography

- wires. *Nanotechnology*, 22(18):185307, May 2011.  
WOS:000288653300010.
- [BZH12] Omar Bobes, Kun Zhang, and Hans Hofsäss. Ion beam induced surface patterns due to mass redistribution and curvature-dependent sputtering. *Physical Review B*, 86(23):235414, December 2012.
- [CW65] J. W. Corbett and G. D. Watkins. Production of Di-vacancies and Vacancies by Electron Irradiation of Silicon. *Physical Review*, 138(2A):A555–A560, April 1965.
- [DDP<sup>+</sup>04] T. van Dillen, M. J. A. de Dood, J. J. Penninkhof, A. Polman, S. Roorda, and A. M. Vredenberg. Ion beam-induced anisotropic plastic deformation of silicon microstructures. *Applied Physics Letters*, 84(18):3591–3593, May 2004.
- [Ded95] Gv Dedkov. The Interatomic Interaction Potentials in Radiation Physics. *Physica Status Solidi a-Applications and Materials Science*, 149(2):453–513, June 1995.  
WOS:A1995RH61400001.
- [DO06] Tomasz Dietl and Hideo Ohno. Engineering magnetism in semiconductors. *Materials Today*, 9(11):18–26, November 2006.
- [DPFB01] T. van Dillen, A. Polman, W. Fukarek, and A. van Blaaderen. Energy-dependent anisotropic deformation of colloidal silica particles under MeV Au irradiation. *Applied Physics Letters*, 78(7):910–912, February 2001.

## Bibliography

- [DPKB03] T. van Dillen, A. Polman, C. M. van Kats, and A. van Blaaderen. Ion beam-induced anisotropic plastic deformation at 300 keV. *Applied Physics Letters*, 83(21):4315–4317, November 2003.
- [Eck91] Wolfgang Eckstein. *Computer Simulation of Ion-Solid Interactions*. Springer Berlin Heidelberg, Berlin, Heidelberg, 1991.
- [FH13] Brent Fultz and James Howe. *Transmission Electron Microscopy and Diffractometry of Materials*. Graduate Texts in Physics. Springer Berlin Heidelberg, Berlin, Heidelberg, 2013.
- [Fur88] J. K. Furdyna. Diluted magnetic semiconductors. *Journal of Applied Physics*, 64(4):R29–R64, August 1988.
- [GHB<sup>+</sup>13] G. Greaves, J. A. Hinks, P. Busby, N. J. Mellors, A. Ilinov, A. Kuronen, K. Nordlund, and S. E. Donnelly. Enhanced Sputtering Yields from Single-Ion Impacts on Gold Nanorods. *Physical Review Letters*, 111(6):065504, August 2013. 00004.
- [Gla15] Markus Glaser. *Personal communication, Thesis in writing*. PhD thesis, TU Wien, Wien, 2015.
- [Gou09] Brian Gough, editor. *GNU Scientific Library Reference Manual - Third Edition*. Network Theory Ltd., s.l., 3rd revised edition edition edition, January 2009.
- [Hau84] M. Hautala. Nuclear stopping in polycrystalline materials: Range distributions and Doppler-shift atten-

## Bibliography

- uation analysis. *Physical Review B*, 30(9):5010–5018, November 1984. 00059.
- [HCA02] Xiaoyuan Hu, David G. Cahill, and Robert S. Averback. Burrowing of Pt nanoparticles into SiO<sub>2</sub> during ion-beam irradiation. *Journal of Applied Physics*, 92(7):3995–4000, October 2002.
- [HKW04] André Hedler, Siegfried Ludwig Klaumünzer, and Werner Wesch. Amorphous silicon exhibits a glass transition. *Nature Materials*, 3(11):804–809, November 2004.
- [HKW05] A. Hedler, S. Klaumünzer, and W. Wesch. Boundary effects on the plastic flow of amorphous layers during high-energy heavy-ion irradiation. *Physical Review B*, 72(5):054108, August 2005.
- [HZM14] H. Hofssäss, K. Zhang, and A. Mutzke. Simulation of ion beam sputtering with SDTrimSP, TRIDYN and SRIM. *Applied Surface Science*, 310:134–141, August 2014.
- [JBB<sup>+</sup>12] C. Jeynes, M. J. Bailey, N. J. Bright, M. E. Christopher, G. W. Grime, B. N. Jones, V. V. Palitsin, and R. P. Webb. ”Total IBA” - Where are we? *Nuclear Instruments & Methods in Physics Research Section B-Beam Interactions with Materials and Atoms*, 271:107–118, January 2012. WOS:000299986500018.
- [JHMR15] Andreas Johannes, Henry Holland-Moritz, and Carsten Ronning. Ion beam irradiation of nanostructures: sputtering, dopant incorporation, and dynamic annealing.

## Bibliography

- Semiconductor Science and Technology*, 30(3):033001, March 2015.
- [JNP<sup>+</sup>14] A. Johannes, S. Noack, W. Paschoal, S. Kumar, D. Jacobsson, H. Pettersson, L. Samuelson, K. A. Dick, G. Martinez-Criado, M. Burghammer, and C. Ronning. Enhanced sputtering and incorporation of Mn in implanted GaAs and ZnO nanowires. *Journal of Physics D-Applied Physics*, 47(39):394003, October 2014. WOS:000341772000005.
- [JNW<sup>+</sup>15] Andreas Johannes, Stefan Noack, Werner Wesch, Markus Glaser, Alois Lugstein, and Carsten Ronning. Anomalous Plastic Deformation and Sputtering of Ion Irradiated Silicon Nanowires. *Nano Letters*, May 2015.
- [Kik28] Seishi Kikuchi. Diffraction of Cathode Rays by Mica. *Proceedings of the Imperial Academy*, 4(6):271–274, 1928.
- [Kla04] S. Klaumünzer. Ion hammering of silica colloids. *Nuclear Instruments and Methods in Physics Research Section B: Beam Interactions with Materials and Atoms*, 215(3–4):345–352, February 2004.
- [KPJ<sup>+</sup>13] Sandeep Kumar, Waldomiro Paschoal, Andreas Johannes, Daniel Jacobsson, Christian Borschel, Anna Pertsova, Chih-Han Wang, Maw-Kuen Wu, Carlo M. Canali, Carsten Ronning, Lars Samuelson, and Håkan Pettersson. Magnetic Polarons and Large Negative Magnetoresistance in GaAs Nanowires Implanted with Mn Ions. *Nano Letters*, 13(11):5079–5084, 2013.

## Bibliography

- [LSH<sup>+</sup>08] A. Lugstein, M. Steinmair, Y. J. Hyun, G. Hauer, P. Pongratz, and E. Bertagnolli. Pressure-induced orientation control of the growth of epitaxial silicon nanowires. *Nano Letters*, 8(8):2310–2314, August 2008. WOS:000258440700034.
- [Luk72] F. Lukeš. Oxidation of Si and GaAs in air at room temperature. *Surface Science*, 30(1):91–100, March 1972.
- [LW07] Charles M. Lieber and Zhong Lin Wang. Functional nanowires. *Mrs Bulletin*, 32(2):99–108, February 2007. WOS:000244600800011.
- [Mü09] Sven Müller. *Structural and optical impact of transition metal implantation into zinc oxide single crystals and nanowires*. PhD thesis, Georg-August Universität Göttingen, Göttingen, 2009.
- [Mö14] Wolfhard Möller. TRI3dyn – Collisional computer simulation of the dynamic evolution of 3-dimensional nanostructures under ion irradiation. *Nuclear Instruments and Methods in Physics Research Section B: Beam Interactions with Materials and Atoms*, 322:23–33, March 2014. 00001.
- [MA03] S. G. Mayr and R. S. Averback. Effect of ion bombardment on stress in thin metal films. *Physical Review B*, 68(21):214105, December 2003.
- [MAAA03] S. G. Mayr, Y. Ashkenazy, K. Albe, and R. S. Averback. Mechanisms of Radiation-Induced Viscous Flow: Role of Point Defects. *Physical Review Letters*, 90(5):055505, February 2003.

## Bibliography

- [ME84] W. Möller and W. Eckstein. Tridyn — A TRIM simulation code including dynamic composition changes. *Nuclear Instruments and Methods in Physics Research Section B: Beam Interactions with Materials and Atoms*, 2(1–3):814–818, March 1984.
- [MEB88] W. Möller, W. Eckstein, and J. P. Biersack. Tridyn-binary collision simulation of atomic collisions and dynamic composition changes in solids. *Computer Physics Communications*, 51(3):355–368, November 1988. 00441.
- [MK97] Antonio Miotello and Roger Kelly. Revisiting the thermal-spike concept in ion-surface interactions. *Nuclear Instruments and Methods in Physics Research Section B: Beam Interactions with Materials and Atoms*, 122(3):458–469, February 1997.
- [MKKP08] S. Massl, H. Köstenbauer, J. Keckes, and R. Pippan. Stress measurement in thin films with the ion beam layer removal method: Influence of experimental errors and parameters. *Thin Solid Films*, 516(23):8655–8662, October 2008.
- [MVB<sup>+</sup>06] J. Meijer, T. Vogel, B. Burchard, I. W. Rangelow, L. Bischoff, J. Wrachtrup, M. Domhan, F. Jelezko, W. Schnitzler, S. A. Schulz, K. Singer, and F. Schmidt-Kaler. Concept of deterministic single ion doping with sub-nm spatial resolution. *Applied Physics a-Materials Science & Processing*, 83(2):321–327, May 2006. WOS:000236641800028.

## Bibliography

- [Nas08] Nastasi/Mayer/Hirvonen. *Ion-Solid Interactions: Fundamentals and Applications.* Cambridge University Press, Cambridge ; New York, auflage: revised. edition, January 2008.
- [ND08] Kai Nordlund and Sergei L. Dudarev. Interatomic potentials for simulating radiation damage effects in metals. *Comptes Rendus Physique*, 9(3–4):343–352, April 2008.
- [NGA<sup>+</sup>98] K. Nordlund, M. Ghaly, R. S. Averback, M. Caturla, T. Diaz de la Rubia, and J. Tarus. Defect production in collision cascades in elemental semiconductors and fcc metals. *Physical Review B*, 57(13):7556–7570, April 1998.
- [NKA<sup>+</sup>04] Nick S. Norberg, Kevin R. Kittilstved, James E. Amontette, Ravi K. Kukkadapu, Dana A. Schwartz, and Daniel R. Gamelin. Synthesis of Colloidal Mn<sup>2+</sup>:ZnO Quantum Dots and High-TC Ferromagnetic Nanocrystalline Thin Films. *Journal of the American Chemical Society*, 126(30):9387–9398, August 2004.
- [Noa14] Stefan Noack. *Sputter Effects of Silicon Nanowires under Ion Bombardment.* University Jena, Master Thesis, 2014.
- [Nor95] K. Nordlund. Molecular dynamics simulation of ion ranges in the 1–100 keV energy range. *Computational Materials Science*, 3(4):448–456, March 1995. 00248.
- [Nor14] Kai Nordlund. Correction to the Kinchin-Phase damage equation to account for athermal defect recombi-

## Bibliography

- nation and ion beam mixing: arc-dpa and rpa. In *Oral Presentation*, Leuven, September 2014.
- [NRS97] K. Nordlund, N. Runeberg, and D. Sundholm. Repulsive interatomic potentials calculated using Hartree-Fock and density-functional theory methods. *Nuclear Instruments & Methods in Physics Research Section B-Beam Interactions with Materials and Atoms*, 132(1):45–54, October 1997. WOS:A1997YF32200007.
- [NSUM14] Maureen L. Nietiadi, Luis Sandoval, Herbert M. Urbassek, and Wolfhard Möller. Sputtering of Si nanospheres. *Physical Review B*, 90(4):045417, July 2014.
- [Ogr13] Matthias Ogrisek. *Kontrolliertes Wachstum von Zinkoxid und Vanadium(IV)-oxid Nanodrähten*. University Jena, Master Thesis, 2013.
- [Ohd08] Iwao Ohdomari. Single-ion irradiation: physics, technology and applications. *Journal of Physics D: Applied Physics*, 41(4):043001, February 2008.
- [Ots79] NOBUYUKI Otsu. A Threshold Selection Method from Gray-Level Histograms. *IEEE Transactions on Systems, Man, and Cybernetics*, 9(1):62–66, 1979.
- [PGB13] D. Primetzhofer, D. Goebel, and P. Bauer. Local vs. non-local energy loss of low energy ions: Influence of charge exchange processes in close collisions. *Nuclear Instruments and Methods in Physics Research Section B: Beam Interactions with Materials and Atoms*, 317, Part A:8–12, December 2013.

## Bibliography

- [PGL<sup>+</sup>14] Slawomir Prucnal, Markus Glaser, Alois Lugstein, Emmerich Bertagnolli, Michael Stoeger-Pollach, Shengqiang Zhou, Manfred Helm, Denis Reichel, Lars Rebohle, Marcin Turek, Jerzy Zuk, and Wolfgang Skorupa. III-V semiconductor nanocrystal formation in silicon nanowires via liquid-phase epitaxy. *Nano Research*, 7(12):1769–1776, December 2014. WOS:000346641400006.
- [PKB<sup>+</sup>12] Waldomiro Paschoal, Sandeep Kumar, Christian Borschel, Phillip Wu, Carlo M. Canali, Carsten Ronning, Lars Samuelson, and Hakan Pettersson. Hoping Conduction in Mn Ion-Implanted GaAs Nanowires. *Nano Letters*, 12(9):4838–4842, September 2012. WOS:000308576000069.
- [PKJ<sup>+</sup>14] W. Paschoal, Sandeep Kumar, D. Jacobsson, A. Johannesson, V. Jain, C. M. Canali, A. Pertsova, C. Ronning, K. A. Dick, L. Samuelson, and H. Pettersson. Magnetoresistance in Mn ion-implanted GaAs:Zn nanowires. *Applied Physics Letters*, 104(15):153112, April 2014. WOS:000335145200060.
- [PMB04] Lourdes Pelaz, Luis A. Marqués, and Juan Barbolla. Ion-beam-induced amorphization and recrystallization in silicon. *Journal of Applied Physics*, 96(11):5947–5976, December 2004.
- [Pri12] D. Primetzhofer. Inelastic energy loss of medium energy H and He ions in Au and Pt: Deviations from velocity proportionality. *Physical Review B*, 86(9):094102, September 2012.

## Bibliography

- [rm15] ITRS road map. ITRS road map, April 2015.
- [Rut11] E Rutherford. The scattering of alpha and beta particles by matter and the structure of the atom. *Philosophical Magazine Series 6*, 21(125):669–688, May 1911.
- [SACF<sup>+</sup>12] Johannes Schindelin, Ignacio Arganda-Carreras, Erwin Frise, Verena Kaynig, Mark Longair, Tobias Pietzsch, Stephan Preibisch, Curtis Rueden, Stephan Saalfeld, Benjamin Schmid, Jean-Yves Tinevez, Daniel James White, Volker Hartenstein, Kevin Eliceiri, Pavel Tomancak, and Albert Cardona. Fiji: an open-source platform for biological-image analysis. *Nature Methods*, 9(7):676–682, June 2012.
- [San04] B Sankur. Survey over image thresholding techniques and quantitative performance evaluation. *Journal of Electronic Imaging*, 13(1):146, January 2004.
- [SBB97] E. Snoeks, K. S. Boutros, and J. Barone. Stress relaxation in tungsten films by ion irradiation. *Applied Physics Letters*, 71(2):267–269, July 1997.
- [Sch08] François Schietekatte. Fast Monte Carlo for ion beam analysis simulations. *Nuclear Instruments and Methods in Physics Research Section B: Beam Interactions with Materials and Atoms*, 266(8):1880–1885, April 2008.
- [Sch12] Bernd Schmidt. *Ion beams in materials processing and analysis*. Springer, New York, 2012.

## Bibliography

- [Sig69] Peter Sigmund. Theory of Sputtering. I. Sputtering Yield of Amorphous and Polycrystalline Targets. *Physical Review*, 184(2):383–416, August 1969. 03204.
- [Sig73] Peter Sigmund. A mechanism of surface micro-roughening by ion bombardment. *Journal of Materials Science*, 8(11):1545–1553, November 1973.
- [Sig04] Peter Sigmund, editor. *Stopping of Heavy Ions*, volume 204 of *Springer Tracts in Modern Physics*. Springer Berlin Heidelberg, Berlin, Heidelberg, 2004.
- [SN06] Simon M. Sze and Kwok K. Ng. *Physics of Semiconductor Devices*. Wiley-Interscience, Hoboken, N.J, 3 edition edition, October 2006.
- [SPC<sup>+</sup>07] V. A. Solé, E. Papillon, M. Cotte, Ph. Walter, and J. Susini. A multiplatform code for the analysis of energy-dispersive X-ray fluorescence spectra. *Spectrochimica Acta Part B: Atomic Spectroscopy*, 62(1):63–68, January 2007.
- [SPTS12] Daniel Sage, D. Prodanov, J.-Y. Tinevez, and J. Schindelin. ImageJ User & Developer Conference (IUDC’12). 2012.
- [SSK<sup>+</sup>11] Janusz Sadowski, Aloyzas Siusys, Andras Kovacs, Takeshi Kasama, Rafal E. Dunin-Borkowski, Tomasz Wojciechowski, Anna Reszka, and Bogdan Kowalski. GaAs–MnAs nanowires. *physica status solidi (b)*, 248(7):1576–1580, July 2011.

## Bibliography

- [Sti08] Daniel Stichtenoth. *Dimensionseffekte in Halbleiter-nanodrähten*. PhD thesis, Georg-August Universität Göttingen, Göttingen, 2008.
- [SvBvD<sup>+</sup>00] E. Snoeks, A. van Blaaderen, T. van Dillen, C. M. van Kats, M. L. Brongersma, and A. Polman. Colloidal Ellipsoids with Continuously Variable Shape. *Advanced Materials*, 12(20):1511–1514, October 2000.
- [SvBvD<sup>+</sup>01] E Snoeks, A van Blaaderen, T van Dillen, C. M van Kats, K Velikov, M. L Brongersma, and A Polman. Colloidal assemblies modified by ion irradiation. *Nuclear Instruments and Methods in Physics Research Section B: Beam Interactions with Materials and Atoms*, 178(1–4):62–68, May 2001.
- [SW85] Frank H. Stillinger and Thomas A. Weber. Computer simulation of local order in condensed phases of silicon. *Physical Review B*, 31(8):5262–5271, April 1985.
- [TDP92] M. Toulemonde, C. Dufour, and E. Paumier. Transient thermal process after a high-energy heavy-ion irradiation of amorphous metals and semiconductors. *Physical Review B*, 46(22):14362–14369, December 1992.
- [Ter88] J. Tersoff. New empirical approach for the structure and energy of covalent systems. *Physical Review B*, 37(12):6991–7000, April 1988.
- [Tho68] Mw Thompson. Energy Spectrum of Ejected Atoms During High Energy Sputtering of Gold. *Philosophical Magazine*, 18(152):377–&, 1968. WOS:A1968B525400015.

## Bibliography

- [TR95] H. Trinkaus and A. I. Ryazanov. Viscoelastic Model for the Plastic Flow of Amorphous Solids under Energetic Ion Bombardment. *Physical Review Letters*, 74(25):5072–5075, June 1995.
- [TVM<sup>+</sup>15] Lionel Thome, Gihan Velisa, Sandrine Miro, Aurelien Debelle, Frederico Garrido, Gael Sattonnay, Stamatis Mylonas, Patrick Trocellier, and Yves Serruys. Recovery effects due to the interaction between nuclear and electronic energy losses in SiC irradiated with a dual-ion beam. *Journal of Applied Physics*, 117(10):105901, March 2015. WOS:000351442900074.
- [UBNM15] Herbert M. Urbassek, R. Mark Bradley, Maureen L. Nietiadi, and Wolfhard Möller. Sputter yield of curved surfaces. *Physical Review B*, 91(16):165418, April 2015.
- [vDSF<sup>+</sup>01] T van Dillen, E Snoeks, W Fukarek, C. M van Kats, K. P Velikov, A van Blaaderen, and A Polman. Anisotropic deformation of colloidal particles under MeV ion irradiation. *Nuclear Instruments and Methods in Physics Research Section B: Beam Interactions with Materials and Atoms*, 175–177:350–356, April 2001.
- [Vol91] C. A. Volkert. Stress and plastic flow in silicon during amorphization by ion bombardment. *Journal of Applied Physics*, 70(7):3521–3527, October 1991.
- [VWMS08] C. Verdeil, T. Wirtz, H. N. Migeon, and H. Scherrer. Angular distribution of sputtered matter under Cs+ bombardment with oblique incidence. *Applied Surface Science*, 255(4):870–873, December 2008.

## Bibliography

- [WDJ<sup>+</sup>09] Brent A. Wacaser, Kimberly A. Dick, Jonas Johansson, Magnus T. Borgström, Knut Deppert, and Lars Samuelson. Preferential Interface Nucleation: An Expansion of the VLS Growth Mechanism for Nanowires. *Advanced Materials*, 21(2):153–165, January 2009.
- [WE64] Rs Wagner and Wc Ellis. Vapor-Liquid-Solid Mechanism of Single Crystal Growth ( New Method Growth Catalysis from Impurity Whisker Epitaxial + Large Crystals Si E ). *Applied Physics Letters*, 4(5):89–&, 1964. WOS:A19645163A00003.
- [WHB77] W. D. Wilson, L. G. Haggmark, and J. P. Biersack. Calculations of nuclear stopping, ranges, and straggling in the low-energy region. *Physical Review B*, 15(5):2458–2468, March 1977.
- [WKW04] W. Wesch, A. Kamarou, and E. Wendler. Effect of high electronic energy deposition in semiconductors. *Nuclear Instruments & Methods in Physics Research Section B-Beam Interactions with Materials and Atoms*, 225(1-2):111–128, August 2004. WOS:000223792600010.
- [WWS12] W. Wesch, E. Wendler, and C. S. Schnohr. Damage evolution and amorphization in semiconductors under ion irradiation. *Nuclear Instruments and Methods in Physics Research Section B: Beam Interactions with Materials and Atoms*, 277:58–69, April 2012. 00009.
- [XYS<sup>+</sup>03] Y. Xia, P. Yang, Y. Sun, Y. Wu, B. Mayers, B. Gates, Y. Yin, F. Kim, and H. Yan. One-Dimensional Nano-

## Bibliography

- structures: Synthesis, Characterization, and Applications. *Advanced Materials*, 15(5):353–389, March 2003.
- [YS84] Y. Yamamura and Shigeru Shindo. An empirical formula for angular dependence of sputtering yields. *Radiation Effects*, 80(1-2):57–72, January 1984.
- [Zie12] James Ziegler. *SRIM - The Stopping and Range of Ions in Matter*. February 2012.
- [ZLB85] J. F. (James F. ) Ziegler, U. Littmark, and J. P. Biersack. *The stopping and range of ions in solids / J.F. Ziegler, J.P. Biersack, U. Littmark*. The Stopping and ranges of ions in matter ; v. 1. Pergamon, New York, 1985. Includes index. Bibliography: p. 308-315.